Polymer Reviews
Publication details, including instructions for authors and subscription information:
http://www.tandfonline.com/loi/lmsc20

Probing Soft Matter with the Atomic Force Microscopies: Imaging and Force Spectroscopy

Michael E. McConney [a], Srikanth Singamaneni [a] & Vladimir V. Tsukruk [a]

[a] School of Materials Science and Engineering, Georgia Institute of Technology, Atlanta, Georgia

To cite this article: Michael E. McConney, Srikanth Singamaneni & Vladimir V. Tsukruk (2010): Probing Soft Matter with the Atomic Force Microscopies: Imaging and Force Spectroscopy, Polymer Reviews, 50:3, 235-286

To link to this article: http://dx.doi.org/10.1080/15583724.2010.493255

Polymer Reviews, 50:235–286, 2010

ISSN: 1558-3724 print / 1558-3716 online
DOI: 10.1080/15583724.2010.493255

Reviews

Probing Soft Matter with the Atomic Force Microscopies: Imaging and Force Spectroscopy

MICHAEL E. McCONNEY, SRIKANTH SINGAMANENI, AND VLADIMIR V. TSUKRUK

School of Materials Science and Engineering, Georgia Institute of Technology, Atlanta, Georgia

The development of atomic force microscopy has evolved into a wide variety of microscopy and characterization techniques well beyond conventional imaging. The focus of this review is on characterization methods based on the scanning probe and their application in characterizing physical properties of soft materials. This consideration is broken into three major categories focusing on mechanical, thermal, and electrical/magnetic properties in addition to a brief review of high-resolution imaging. Surface spectroscopy is discussed to great extent and consideration includes procedural information, common pitfalls, capabilities, and their practical application in characterizing soft matter. Key examples of the method are presented to communicate the capabilities and impact that probe-based characterization techniques have had on the mechanical, thermal, and electrical characterization of soft materials.

Keywords atomic force microscopy, force spectroscopy, scanning thermal microscopy, kelvin probe force microscopy, scanning probe microscopy, polymers

1. Introduction to Atomic Force Microscopy Imaging

The invention of scanning tunneling microscopy (STM) in early 1980 by Rohrer and Binnig at the IBM Zurich Laboratories led to a fast establishment of a new class of microscopy known as *scanning probe microscopy* (SPM) over the past three decades.[1–6] Overcoming the limitations of STM in their application to nonconductive materials, atomic force microscopy (AFM) was introduced as a logical next step in SPM techniques, thereby greatly expanding the imaging and probing capabilities.[7] The ongoing development of SPM and nanotechnology remain deeply intertwined and mutually augmented.

SPM techniques have several common components, including an ultrasharp probe, sensing elements (Figure 1A), a piezo scanner tube, and a computer-controlled feedback

Received January 20, 2010; accepted April 21, 2010.
Address correspondence to Vladimir V. Tsukruk, School of Materials Science and Engineering, Georgia Institute of Technology, 771 Ferst Dr., Atlanta, GA 30332-0245. E-mail: vladimir@mse.gatech.edu

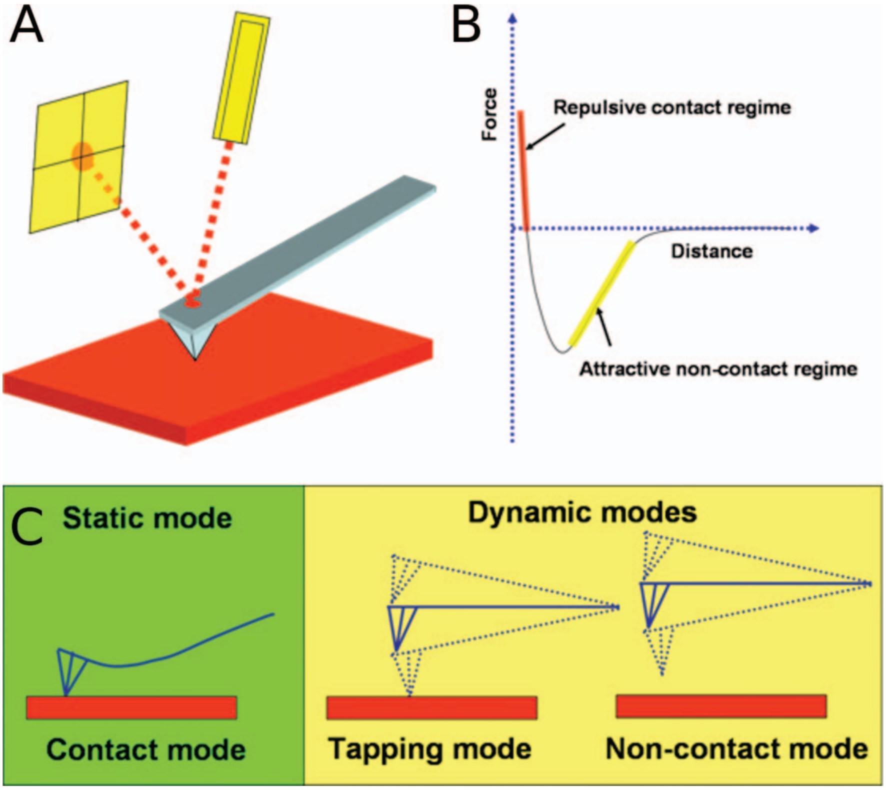

Figure 1. (a) Schematic depicting the AFM tip interacting with the sample surface and the most common optical technique employed to detect the deflection of the microcantilever. (b) Interaction force–separation distance plot showing the long range attractive regime (noncontact) and short-range repulsive regime (contact). (c) Schematic showing the microcantilever interaction with the sample in the three basic imaging modes of operation of AFM.

loop. One key feature that set SPM-based techniques apart from other microscopy techniques is the use of ultrasharp probes. Apart from imaging the properties with nanoscale resolution, one of the important developments is the manipulation of matter on the surface using a scanning probe. Furthermore, as natural succession to their application as force transducers in AFM, microcantilevers are being extensively investigated as a new platform for transduction in sensing technology in chemical, biological, and thermal sensing.[8–13]

The unprecedented lateral and vertical resolution offered by SPM techniques enables the visualization of micro-, nano-, and molecular-scale structure of polymer surfaces and interfaces. Under special conditions, atomic resolution is even attainable with SPM.[14] Other outstanding advantages of SPM include true three-dimensional (3D) topology, minimal sample preparation, and imaging under a wide variety of environments, including ambient conditions, fluidic conditions, gases, and under different temperatures. Various SPM techniques enable simultaneous probing of the different properties, such as structural, mechanical, electrical, thermal, or magnetic properties with nanoscale resolution. These microscopy methods continue to provide invaluable insight into the understanding structure–property relationship of these materials at nanoscale. SPM can be used to manipulate and pattern soft matter by applying normal and shearing forces and modifying surface topography by repeated scanning.[15,16]

Based on cantilever dynamics, AFM operation can be generally divided into static and dynamic modes as shown in Figure 1C. Dynamic modes involve oscillating the cantilever, usually near its resonance frequency. Under dynamic modes, the resonant frequency, amplitude, and phase of the oscillation change due to the interaction between the tip and the sample. Dynamic modes can be carried out in several variations including amplitude modulation (AM-AFM) and/or frequency modulation (FM-AFM). The most common type of dynamic mode AFM, called *tapping mode* or *intermittent contact*, is a simple and robust amplitude-modulated AM-AFM technique. On the other hand, in the static mode, the tip is raster-scanned across the surface and the deflection of the cantilever is maintained constant by the feedback control. The readers are referred to several reviews for detailed information regarding AFM-based imaging and discussion of static and dynamic modes.[17,18]

Under ambient conditions the magnitude of the tip-to-sample force in the contact mode is typically between 1 and 100 nN. This force for a regular tip (radius of few nanometers) results in a pressure of few GPa, which is on the order of yield stress of glassy polymers, thus often causing plastic deformation. On the other hand, the forces are greatly reduced to 0.1–1 nN by performing the scanning in fluid (water, organic solvents, etc.) because the capillary forces are significantly minimized. Overall, imaging in contact mode involves relatively large shear forces, frequently resulting in the damage and distortion of soft surfaces, making it unfavorable for polymeric and biological samples and it is thus employed only in some special cases (e.g., for friction force microscopy, see below).

In order to prevent surface damage caused by contact imaging, noncontact modes were developed.[19,20] Generally, noncontact modes operate with the probe scanning about 5–40 nm above the sample surface, perturbed by the attractive van der Waals forces between the tip and the sample; see Figure 1B. In order to overcome the limitation of the relatively weak tip–sample interaction force observed under static noncontact mode, the cantilever is set to oscillate at or slightly off of the resonance frequency of the cantilever. The lateral resolution of the dynamic mode is typically limited to 0.5 nm for topography and around 10 nm for other properties.

Dynamic modes can reduce the typical operational forces by at least one order of magnitude compared to the contact mode (usually well below 1 nN). It virtually eliminates the shear force associated with the lateral raster scanning and reduces the tip sample contact duration by two orders of magnitude. Noncontact modes have been applied for studying a wide variety of materials such as metals, semiconductors, polymers, and biological materials. These modes offer unique advantages for probing the soft polymeric and biological samples compared to contact AFM.

Although in a practical version of noncontact mode, so-called tapping mode, forces are considered minimal, they are nonetheless substantial and might result in surface modification and damage, especially in hard tapping.[21] In general, the phase shift at modest tapping forces is proportional to the stiffness of a material, but stiffness is dependent on the contact radius, which is generally larger for softer materials under the same forces. On the other hand, these tip–surface contact area issues are less important under medium-tapping forces, compared to hard tapping forces. Furthermore, because the tip–surface contact area can significantly affect the phase shift angle, it is important to consider the effects of topography when interpreting phase images.[22]

To date, tapping mode has been extensively employed for imaging a wide variety of polymer surfaces such as hard, glassy polymers; crystalline polymers; rubbers; gels; polymer fibers; polymer blends; block copolymers; and polymer composites. Apart from tracking the surface topography using the weak van der Waals forces, noncontact dynamic mode is employed for probing other weak forces such as electrostatic and magnetic, as discussed later.

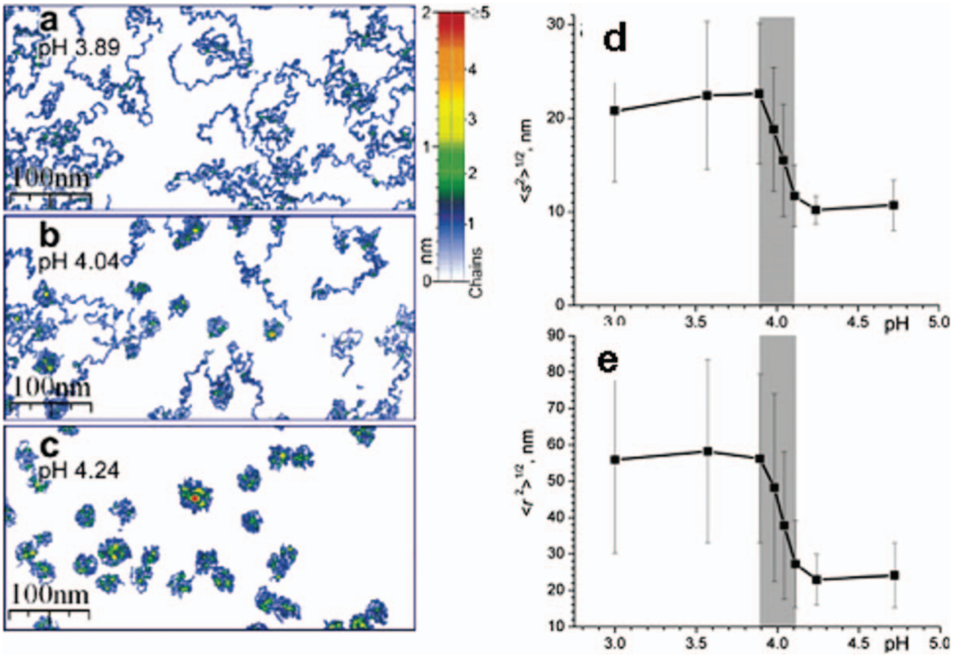

Figure 2. AFM images revealing the conformations of adsorbed P2VP chains: (a) pH 3.89, extended coils; (b) pH 4.04, intermediate state; (c) pH 4.24, compact coils. Plots depicting the (d) RMS end-to-end distance and (e) RMS radius of gyration of P2VP single molecules adsorbed on mica surface versus pH. (Obtained from Roiter and Minko[29] with permission from the American Chemical Society.)

One common approach to using lift mode involves a special raster scan where each line is scanned twice before the next line is scanned. In the first line scan, the topography is scanned in a conventional manner, such as tapping mode, and then the probe is lifted by a set amount (several nanometers) and the probe retraces the previous topographic line scan, which thereby effectively eliminates the topographical contributions to these other signals. For comprehensive review of the basic AFM modes of imaging and their application to the various classes of polymers the readers are referred to corresponding reviews and books on the subject.[6,17,18,23–28]

One very recent notable study was the use of AFM for revealing the conformation of a single polymer chain directly in fluid.[29] Using light tapping mode (98% free amplitude) imaging under controlled pH, Minko et al. observed the conformation change in poly(2-vinylpyridine) (P2VP) chains adsorbed on atomically flat mica substrates (Figures 2A–C). The P2VP chains exhibited a sharp globule to coil transition with a change in the pH from 4.0 to 3.8. Analysis of the AFM images clearly revealed that the protonation of the P2VP chains (with change in pH) dramatically altered the RMS end-to-end distance and the radius of gyration (Figures 2D and E).[29]

Tsukruk and coworkers have performed ambient and in-fluid tapping mode imaging of the surface morphology of the mixed covalently grafted brush layer about 5 nm thick composed of Y-shaped binary molecules polystyrene (PS) and poly-(acrylic acid) (PAA; Figure 3).[30,31] The surface topography images revealed the nanoscale network-like surface morphology formed by coexisting stretched soluble PAA arms and collapsed insoluble PS chains in water. Exposure to different fluids (selective solvents for individual or either

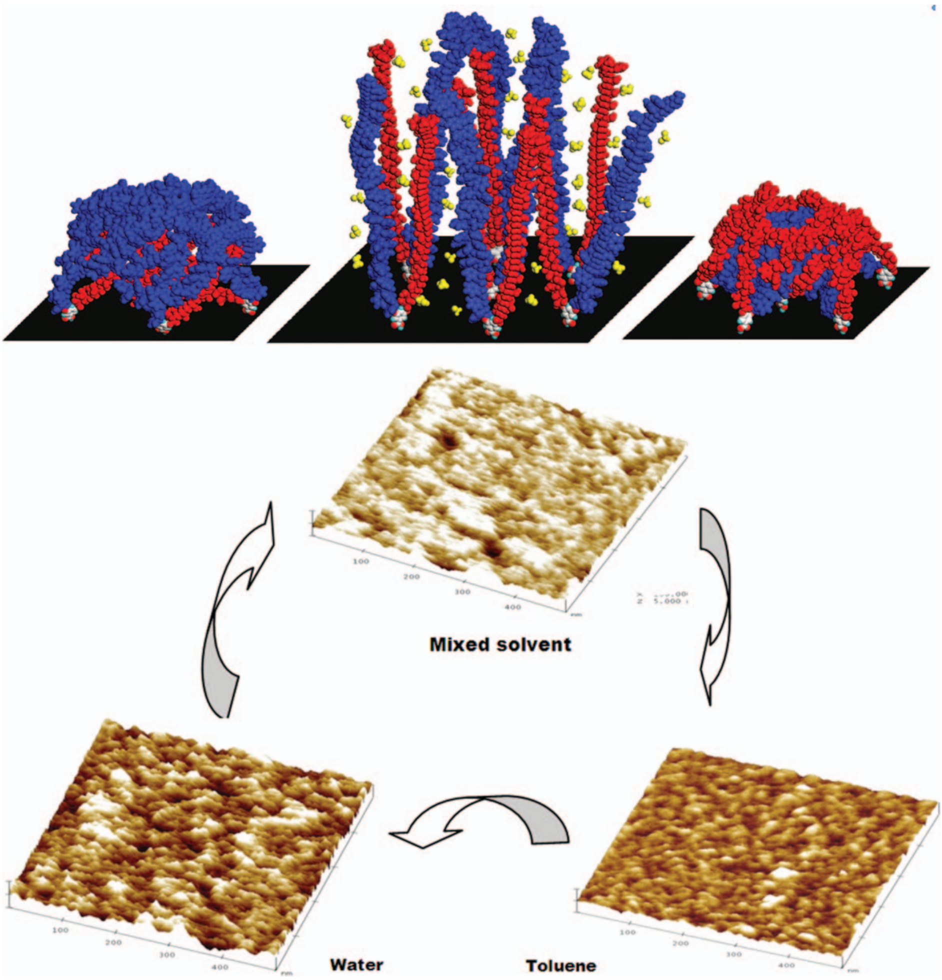

Figure 3. Top: Schematics of molecular transformations and AFM images of Y-shaped amphiphilic brushes combining two dissimilar hydrophobic and hydrophilic polymer chains (polystyrene [PS] and poly-(acrylic acid) [PAA]). Bottom: AFM images collected in light tapping mode in different solvents. The images clearly reveal the switching surface morphology depending on the quality of the solvent for individual components of the mixed brushes (adapted from Lin et al.[32] Copyright American Chemical Society).

blocks) resulted in dramatic reorganization of the Y-shaped brushes. The structural organization of the brushes ranged from a soft repellent layer covered by swollen PS arms in toluene to an adhesive, mixed layer composed of coexisting swollen PAA and collapsed PS arms in water (Figure 3).[32]

The motion of macromolecules, polymers, and biomolecules can be observed in real time with AFM.[33–37] This technique has been particularly useful in observing the molecular motion mechanisms of proteins. This technique has also been used to observe the reputation of polymers. The reptation of isolated isotactic poly(methyl methacrylate) (it-PMMA) chains deposited on a mica substrate was imaged in the tapping mode (Figure 4). The thin water layer (0.1 nm) adsorbed on the substrate accelerated the reptation movements. The reptation movements were also observed in the noncontact mode (frequency modulation

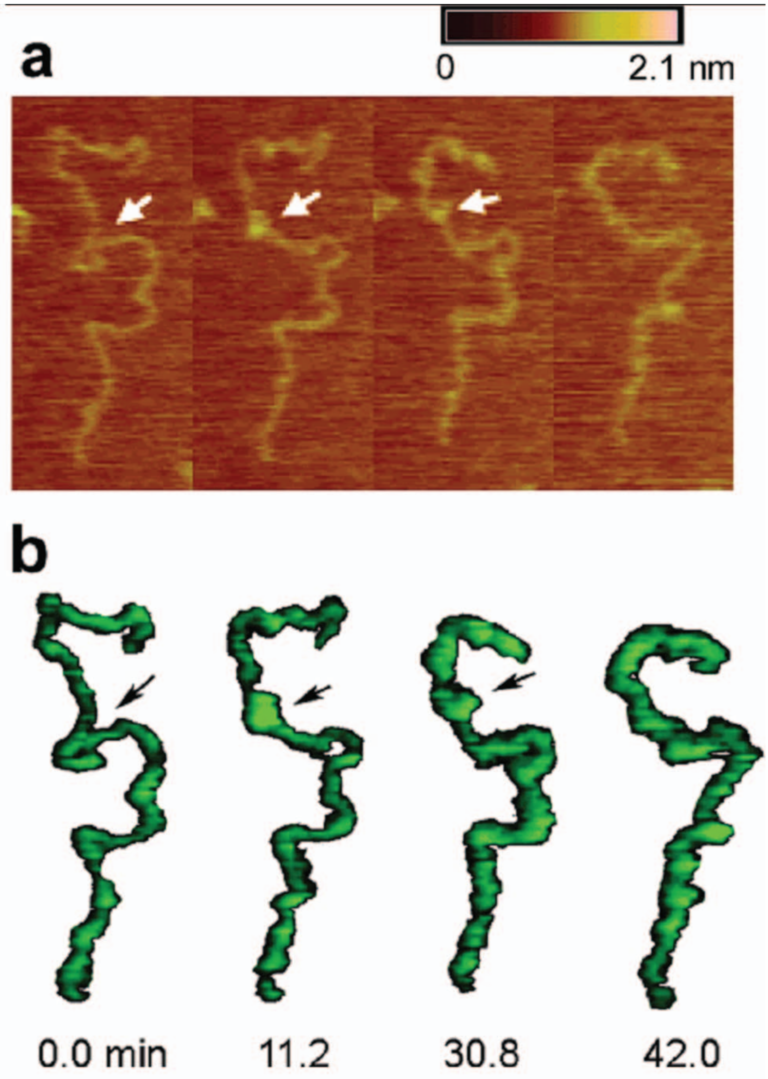

Figure 4. 2D (top row) and 3D (bottom row) time-lapse AFM images showing the movements of an isotactic-PMMA chain on mica at lower humidity (34% RH). The arrow indicates movements of a loop along the chain. (Obtained from Kumaki et al.[38] with permission from the American Chemical Society.)

mode) in which the tip force acting on the chains is smaller compared to that in the tapping mode.[38] Figure 4 shows the detailed conformational changes of it-PMMA chains at 34% RH. The loop indicated by the arrow in the AFM image moved along the chain as shown by the 2D (top) and 3D (bottom) AFM in Figure 4.

Though conventional AFM microscopy modes offer unprecedented vertical and lateral resolution, these techniques provide no information about subsurface features, except in the case of features very shallowly buried below the surface. Subsurface features (defects, fillers, and the like) can be nondestructively imaged using methods based on acoustic microscopy in which an acoustic (ultrasonic) wave is transmitted through the sample and the amplitude and phase of the acoustic wave are monitored to image the subsurface features.

Ultrasonic force microscopy (UFM) is a robust technique developed for subsurface imaging and can be considered as a modification of the standard contact mode of AFM where the sample is oscillated at a high frequency (compared to the resonance frequency of the cantilever) by an additional piezo-resonator.[39,40] The microcantilever exhibits nearly 10^2–10^4 times higher dynamic stiffness at frequencies much higher than the primary resonance frequency. The fundamental principle involves working in the inertial regime (high dynamic stiffness) of the cantilever and sensing the nonlinearity of the tip surface interaction. The sample oscillating at these higher frequencies exerts a constant additional force on the apparently stiff cantilever, elastically indenting itself into the tip. The modulation of ultrasonic waves passing through the sample thickness due to the varying local stiffness and buried features are detected as modulation of the cantilever deflection. Apart from subsurface imaging, UFM has been employed to probe the local mechanical properties of thin polymer films and composites, especially materials with high elastic moduli.[41,42]

A major issue with UFM for imaging the subsurface features is the nonlinear tip–sample interaction, which is extremely sensitive to the elastic and viscoelastic properties of the surface. Furthermore, the method is not ideal choice for soft polymeric and biological samples due to the relatively large forces of interaction between the tip and the sample. Overcoming these limitations, scanning near-field ultrasound holography (SNFUH) has been developed in which two ultrasonic waves are setup one from underneath the sample (2.1 MHz) and the other from the cantilever (2.3 MHz), forming a standing wave.[43] The phase and amplitude of the sample scattered ultrasound wave, manifested as perturbation to the surface acoustic standing wave, are mapped to unveil the subsurface features.

2. Mechanical Characterization of Polymer Surfaces

The AFM is capable exerting and detecting forces orders of magnitude lower than that of the chemical bonds.[44] The photodetector has sub-Angstrom sensitivity, resulting in the theoretical ability to measure forces down to 0.1 pN, but noise from thermal, electronic, and optical sources limits the force sensitivity in ambient conditions to about 1 pN, with practical limits closer to 5 pN.[44] Therefore, it should be should be quite evident that AFM has the potential to address materials and molecules with minimal forces over minimal surface areas. This part has a major section dedicated to force spectroscopy due to the ubiquitous nature of this method and because there are several techniques that use common fundamentals related to force spectroscopy.

2.1. Probes for Characterizing Mechanical Properties

Regular AFM probes are fabricated from silicon or silicon nitride with typical radii of 10–20 and 20–30 nm, respectively. Silicon nitride probes are preferred for very stiff surfaces (the elastic modulus higher than 3 GPa). For these probes, at regular forces exerted during probing mechanical properties the diameter of the contact area usually does not exceed 1–3 nm and thus mechanical or adhesive properties can be probed with near-molecular resolution.[45] However, the use of these highly hydrophilic tips is generally feasible for relatively stiff materials (usually with the elastic modulus higher than 1 MPa) with nonhydrophilic and low-adhesive surfaces. In the case of hydrophilic, highly compliant materials (e.g., hydrogels) with sticky surfaces, regular tips are prone to contamination and easy piercing. In these cases, colloidal probes and chemically modified tips should be used.

Colloidal probes are fabricated by carefully gluing microspherical particles onto the end of a tipless cantilever.[46,47] The microparticles are available through several commercial sources and colloidal probes themselves are commercially available as well. Microparticles with a diameter of a few micrometers from silica and borosilicate glass are most commonly used and have roughness below 1 nm for a square micrometer area, acceptable for most measurements of soft materials. Force spectroscopy performed with such probes is usually called *colloidal force spectroscopy* (CFS).

The colloidal probes have several advantages over conventional probes for very compliant materials. A major advantage is that the applied forces per a unit area are significantly lower than conventional probes, thus allowing for probing very compliant materials such as hydrogels with the elastic modulus well below 1 MPa and down to a fraction of kPa and even few Pas.[48] By applying less force per unit area, the total applied force can be much higher without plastically deforming the surface or damaging the probe, which provides higher resolution in force/area per a force curve by sacrificing lateral spatial resolution. It is very important to note that probing depths are highly dependent on the probe radius, and therefore colloidal probes are inappropriate for characterizing the stiffness or elastic modulus of ultrathin compliant films. Furthermore, the microparticle radius quoted by the manufacturer is generally quite accurate compared to conventional probes and can be easily verified with SEM.

The preservation and well-defined tip shape allow for very good analysis with contact mechanics models that assume spherical shape of the probe, such as the Hertzian approximation (see below). However, care should be taken in preparation to ensure good particle–cantilever contact and that the probing particle surface is not covered with glue. It is also possible that the mechanical properties of the glue between the sphere and cantilever can be sampled instead of the sample itself when measuring stiff samples, such as reinforced polymers.

Chemical modification of probes is generally used to enhance or reduce tip–sample interactions, which can be useful for a variety of applications including chemical force microscopy and chain-pulling experiments.[49] Probes are usually modified with self-assembled monolayers (SAMs) with thiol chemistry on gold precoated tips or silane chemistry on native silicon oxide surface. Thiol-based surface modification involves coating tips with an adhesion layer followed by a gold coating. Silane modification can be done directly on silicon and silicon nitride tips after thorough cleaning.[50]

Thiol modification involves noncovalent bonding, which leads to a limited lifetime.[50] Though thiol SAMs are an important tool for surface scientists, they are poor surface modifiers for applications involving relatively high forces, such as contact mode technique. On the other hand, silane-based modifications involve covalent bonds, which are quite robust and long-lasting.[50] Unfortunately, silane modification involves relatively stringent reaction conditions and is somewhat difficult to initially optimize to achieve single monolayer coverage. The reaction is very sensitive to water presence, so the relative humidity has to be limited to a few percent and dry solvents must be used. On the other hand, thiol modification is relatively straightforward and can be conducted under ambient conditions. The ease of thiol tip modification has led to its extensive use even in contact mode and friction modes, causing widespread characteristic artifacts to be generated.

2.2. Force Spectroscopy

2.2.1. Principles of Force Spectroscopy. Surface force spectroscopy (SFS) is a powerful method to probe the nanomechanical and adhesive properties of surfaces, such as quantification of the elastic modulus, adhesion, chemical binding, inter-/intramolecular forces, resilience, elasticity, and more. Modified SFS techniques are also quite useful for electrical and thermal characterization of materials. The so-called pulling-off version of SFS is widely utilized for investigation of protein unfolding, brush stretching, and other tensile-related mechanical properties of individual molecules and requires usually special tip modification with selectively binding groups. Discussion of this approach can be found in some recent papers and reviews and will be not discussed in this review.[49,51–57] AFM-indentation based methods that involve plastic deformation can be used to investigate material properties and material failure mechanisms. Indentation methods offer an alternative to elastic SFS measurements, thereby avoiding the difficulty arising from minimizing applied loads. Although AFM indentation-based measurements are an invaluable tool in polymer material analysis, this subject will not be discussed in this review; the reader is referred to relevant papers and reviews.[58–61]

As a surface-based technique, SFS is well suited to study the effect of free surfaces and confined surfaces on polymeric properties, which can be quite different from bulk properties. Force spectroscopy measurement is a multistep process, which should be done with great care to ensure accurate results and avoid misleading results. Therefore, it is quite important to fully understand the process and the sources of error. Furthermore, like many experimental methods, practice and experience with known samples is invaluable. Every sample behaves somewhat differently and therefore there is usually a learning curve associated with each new sample.[62,63]

A single force–distance curve is a plot of tip–sample force vs. piezoelement movement (Figure 5A). In Figure 5A is an ideal force–distance curve plotted in the conventional trace–retrace manner. The x-axis can be generally understood as the distance between the tip and the surface. First, the vertical piezoelement is moved in the extension direction, which is depicted in the solid line in Figures 5A and B. In the curve, line 1–2 is called the extension zero-line, which corresponds to the region when the sample is not in contact with the tip but is moving toward the probe. Line 2–3 corresponds to the "jump to contact" region (also known as the *snap-to* region), when the probe is initially attracted to the sample surface, thereby bending the cantilever downward. The surface is also deformed slightly toward the tip in the snap-to section of the curve. This snap-to section corresponds to an unstable displacement of the tip, where the movement of the free end of the cantilever cannot be directly related to the movement fixed end and therefore the sample penetration is not directly measured.

The deflection of the cantilever, when in contact with the sample surface, is indicated by line 3–4. In this region, as the piezoelement moves the sample surface closer toward the cantilever, the cantilever passes from being bent downward through the zero deflection to being bent upward. This region is linear for purely elastic deformation with a slope directly related to surface stiffness. For infinitely stiff substrates that are utilized for sensitivity calibration, the slope is 1, which reflects the fact that the cantilever deflection is exactly equal to the piezoelement displacement. In the case of time-dependent surface deformation (viscoelasticity), nonuniform deformation, or plastic deformation this region becomes highly nonlinear.

Point 4 indicates the end of the tip extension sequence and the beginning of the tip retraction sequence. Ideally, lines 3–4 and 4–5 will partially overlap and have the same slope during extension and retraction. Generally, the line 5–6 region represents the force of adhesion, "pulling forces," or the "snap from contact" event. It is vertical in ideal cases but can display complex shapes in special cases (e.g., "sawtooth" shape for multiple chain unfolding events). Piezoelement hysteresis can be noticeable in this region at high

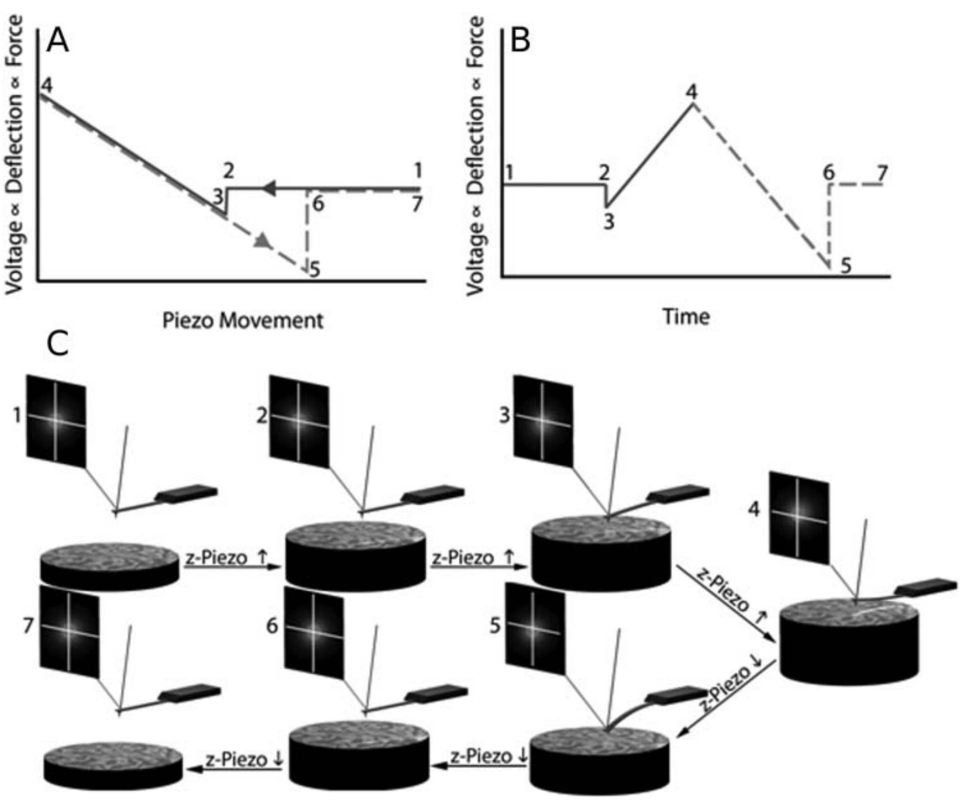

Figure 5. (a) An ideal force–distance curve as explained in the text. (b) The deflection data from (a) plotted with respect to time. (c) A schematic explaining the different regions of the force curve. Note that all the numbers in a–c correspond to each other. It is also important to carefully note that in the schematic, the laser spot, cantilever deflection and sample height (piezoelement position) correspond to their positions of the force curve.

frequencies (tens of Hz) appearing as a small initial upward deflection upon the start of retraction. Line 6–7 is again a region where the cantilever is free from the contact with the surface.

It is important to note that the applied force is indirectly measured by the AFM by relating the photodiode signal to cantilever deflection and relating cantilever deflection to the applied force. The cantilever spring constant must also be calibrated for each set of force measurements. Force spectroscopy mapping (sometimes referred to as *force–volume mode*) is a spatial map of force–distance curves collected across a selected surface area. This force–distance curve matrix can be used for sampling statistics, as well as relating surface features to mechanical properties.

Calibrating the photodiode sensitivity involves obtaining force curves on a material with a stiffness that is much greater than the cantilever stiffness and therefore can be considered "infinitely hard." Typically, a freshly cleaned piece of silicon wafer using piranha solution is employed.[50] Silicon substrates are immersed for 30 min, followed by several washings under deionized water and then drying under filtered dry nitrogen gas. It is important to be stringent with cleaning of the calibration sample, to ensure that no surface contaminants interfere with the accuracy of the photodiode calibration. Error in the photodiode sensitivity causes a shift in all of the data introducing systematic error which can be very significant and requires postmeasurement verification.

The photodiode sensitivity calibration is based on relating the known movement of the vertical piezoelement to the cantilever deflection on stiff substrates (e.g., glass or silicon with the elastic modulus of 170 GPa). Several common pitfalls are related to calibrating the photodiode sensitivity, which are mentioned here. Firstly, it is important to have a freshly cleaned sample to prevent surface contaminants common under conventional lab conditions, which can invalidate the assumption that the penetration is zero.

Another common pitfall is related to the thermal drift of the piezoelement. As measurements are performed, the piezoelement warms and the response of the piezoelement will drift. The piezoelement movement is calibrated when the scanner is warm and therefore the photodiode calibration should also be performed when the scanner is warm. Thermal drift is not a problem for z-closed loop scanners because the piezoelement movement is independently measured. For scanners without z-closed loop, the scanner can be warmed by "exercising" the piezoelement. In order to prevent tip damage the scanner can be exercised in free air by false engaging. To warm the head, one can perform force curves with relatively large ramps in air for 20–30 min to warm the head.

There are several well-developed methods for measuring cantilever spring constants: the most common methods are the added-mass method,[64] geometry-based methods,[65–68] the spring-on-spring method,[69] and the thermal tuning method.[70] Special developments in the form of calibration plots and modified equations have been suggested for more complicated cases such as gold-sputtered silicon nitride cantilevers.[67,71] Although the developed equations are quite good at expressing the spring constant based on the cantilever geometry, there is usually a significant difference between theoretical spring constants and experimentally measured spring constants.[68] The spring-on-spring method can be used to measure cantilever spring constants by performing force curves on a previously calibrated cantilever. This method has good accuracy and can be estimated as roughly 10% when performed with care; it is also relatively easy to perform and is useful in the case when thermal tuning sweep cannot cover the resonance frequency of cantilevers. The thermal tune is generally easier to perform but is not available on all microscopes and for a whole range of relevant frequencies.[72,73]

It is well known that the finite tip-end dimensions (usually within 5–30 nm) distort the feature sizes of images within nanoscale features because of shape convolution (sometimes called *dilation* or *convolution*). Furthermore, tip shape is often the source of common scanning artifacts, such as doubled features or asymmetric tip. Although this is a common imaging problem, in this section we are concerned with tip dimension measurements regarding the tip–sample contact area during force spectroscopy measurements.

The size and shape of the SPM tip must be known to quantify the applied force per area. Several methods have been used to measure the tip size and shape. SEM has been used with relatively good success, although the resolution is practically limited to 2–3 nm. Often the imaging should be performed on conductive tips and the accelerating voltage should be limited to avoid charging. It should also be noted that SEM can often lead to the formation of carbon-based structures on the surface from surface contaminations.

Another common method involves calculating tip dimensions from images obtained by scanning samples with known dimensions under tapping mode (Figure 6). Often the nanoparticles are embedded in a poly-lysine coating or attached to amine-terminated SAM, which when scanned appears to help to remove tip contamination and prevent nanoparticle rolling and detachment. Scanning standard gold nanoparticles of diameters from 5 to 30 nm that are tethered to a modified atomically flat mica or silicon surface has proven to be quite

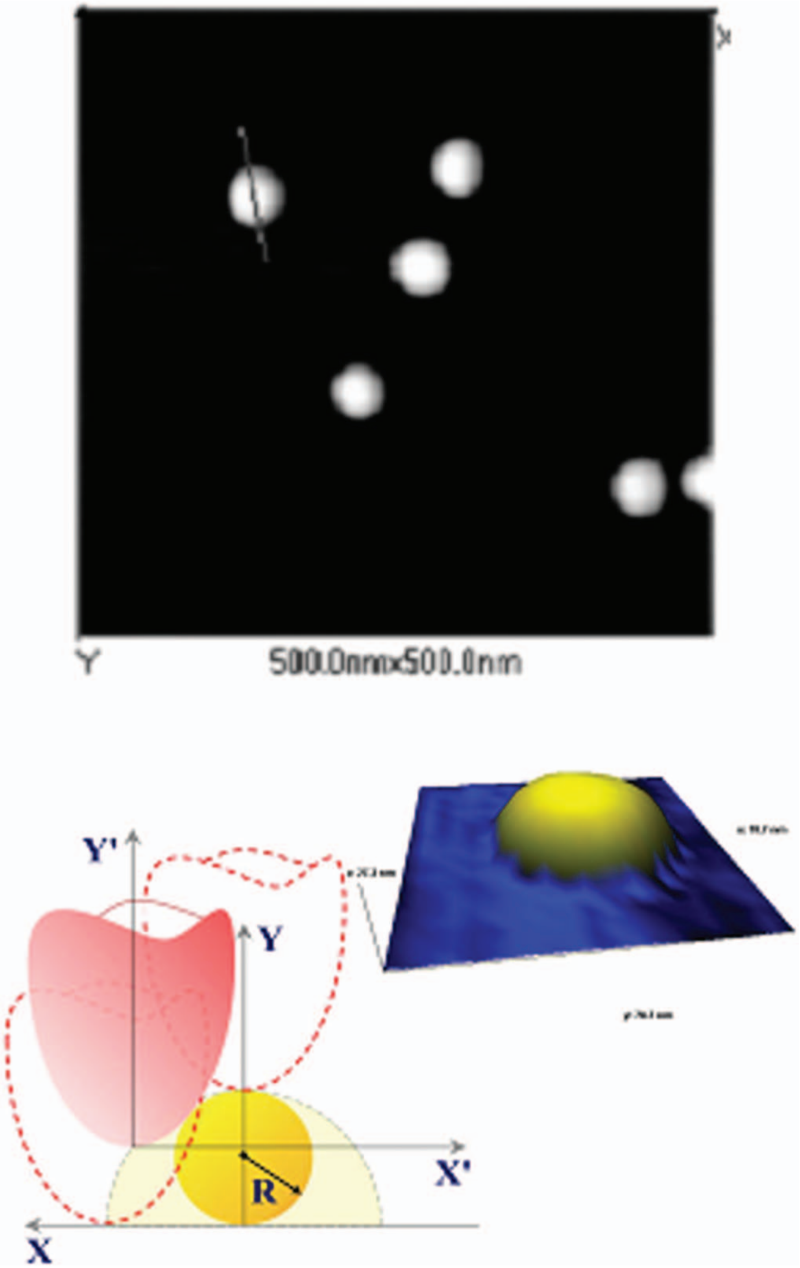

Figure 6. AFM tip deconvolution and dilated image of gold nanoparticle (bottom); AFM image of gold nanoparticles with diameter 20 nm (top).

accurate at characterizing the very end most portion of the tip. The tip can also be characterized with transmission electron microscopy, by measuring the shadow created by the tip with higher resolution. Another method, so-called direct tip imaging, involves scanning microfabricated calibration samples with sharp features available commercially.[74,75]

2.2.2. Elastic Modulus via Force Spectroscopy. A common misconception is that accurate (usually better than ±50%) quantitative elastic modulus data cannot be obtained from force spectroscopy. This belief comes from the inability to measure the tip surface contact radius in real time and a cumbersome, extremely time-consuming experimental routine that is rarely followed properly without devastating shortcuts. Furthermore, the unstable nature of the snap-to region prevents the exact knowledge of the contact point and creates a certain discrepancy in the initial penetration thus affecting a long chain of calculation. Ease of damaging soft surfaces is a common problem for these materials.

Fortunately, for all practical purposes this problem is not as critical or devastating as perceived. Overall, when all steps are performed with care, the resulting data have shown very good agreement with known elastic modulus data for known materials. Overall, quality SFS results should be considered pretty accurate within 20% deviation beyond initial engagement instabilities, as has already been demonstrated for a number of soft materials.[24,76,77]

There are many tasks for which SFS elastic modulus measurements with nanoscale resolution are the only viable option, but other options should always be considered when high spatial resolution is not required, such as buckling-based metrology (BBM).[78] BBM is much less time consuming and has about the same accuracy as SFS. BBM is very appropriate for ultrathin polymeric samples. Furthermore, generally buckling is used for homogenous samples, although in certain cases can be used to measure the modulus of individual components.[79] Freely suspended films can also be characterized using the so-called bulging approach.[80] However, every technique has its own set of limitations and issues to consider.

Nonetheless, if one must use SFS for elastic modulus measurements there are several critical things to do in order to get high-quality quantitative results, including using a cantilever with an appropriate stiffness, stringently avoid tip damage, preventing sample damage, performing calibrations carefully, and analyzing data properly. Although technical steps for these measurements are well known and documented in multiple notes and manuals, here we will list major steps and offer critical evaluations of uncertainties, issues, and important details that are rarely discuss in casual texts. These subjects will be discussed in detail in the following subsections, except for photodetector and sensitivity calibrations, routines that have already been discussed.

2.2.2.1. Choosing Appropriate Cantilever Spring Constants. In order to properly probe the relative stiffness or quantify the elastic modulus of a surface it is imperative to use a probe with an appropriate spring constant–tip radius combination for the sample with particular stiffness. This strict requirement is a product of inherent nature of cantilever-based transduction; specifically, the fact that the applied force (deflection) sensitivity is inversely proportional to the surface deformation (penetration) sensitivity. Relative stiffness and elastic modulus are measures of the penetration versus deflection; therefore, the implication of this seesaw relationship between the sensitivities is that the ideal ratio of deflection to penetration is 1. Furthermore, measurements with deflection-to-penetration ratios of less than 1 or more than 10 results in the stiffness or modulus going to zero or infinity, respectively, because of instrument limitations.

Figure 7 is a generalized graph that indicates the appropriate range of spring constants vs. sample elastic moduli if a standard AFM tip is utilized. This graph is based upon aforementioned criteria verified with actual measurements and is a crude guide for initially choosing the appropriate cantilever spring constants when the elastic modulus can be estimated. This graph is inappropriate for probes with large tip radii, colloidal probes. An

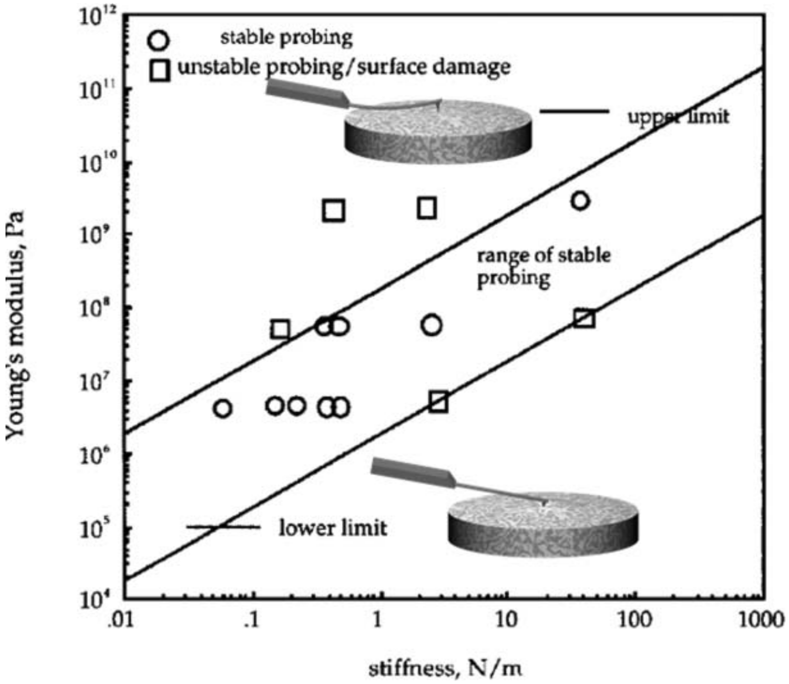

Figure 7. A graph indicating the upper and lower limits of appropriate cantilever spring constants as a function of sample elastic modulus. The top inset shows that the unstable region above the upper limit corresponds to probing where the cantilever deflection is much larger than the sample penetration. The bottom inset shows that the unstable region below the lower limit corresponds to probing where the cantilever deflection is much larger than the sample penetration. (Adapted from Tsukruk et al.[90] Copyright Wiley-Blackwell.)

estimation of the samples' elastic modulus is required to choose an appropriate probe, which adds to the learning curve associated with measuring new samples.

2.2.2.2. Avoiding Tip Damage. Avoiding tip damage is extremely important to obtaining robust quantitative elastic modulus data, because tip–sample contact models typically require hemispherical (or paraboloid) tip shape and the tip radius. Therefore, when small indentation depth and lateral resolution are not critical and specimens are compliant, colloidal probes should be used. Silicon nitride tips are still sharp but much more resilient than silicon tips.

To preserve the tip shape, first, great care should be taken when engaging on surfaces, especially stiffer ones. Engaging in contact mode requires properly setting the difference between the deflection offset and deflection setpoint. The deflection offset is the difference between laser light shined on the top half and bottom half of the quadrant photodiode, measured in units of voltage. The deflection setpoint is a user-defined value, which when engaging is used to define the relative amount of cantilever deflection until the system considers itself engaged. In other words, when engaging, the microscope will continue to move the cantilever toward the sample until the deflection offset matches or exceeds the value of the deflection setpoint. It is important to not engage too hard, or one will destroy the tip. Therefore, the safest approach is to set this difference to be fairly small, which will likely falsely engage the tip at first. Then systematically slightly increase the difference, until the probe properly engages on the surface.

Usually the deflection setpoint is kept at zero and the deflection offset is altered, which helps to ensure that the laser spot is near the center of the photodetector when the cantilever is engaged. Ensuring that the laser spot is in the center of the photodetector is important. Checking for a false engagement is relatively easy, by changing the deflection setpoint by a small amount (∼0.02 V) in contact scanning mode with the x-y range set to zero and checking for a noticeable change in the z-piezoelement position. It should be noted that this check will not work when the tip has been engaged too hard. Proper engagement on the sample should result in the ability to reach the sample with the piezoelement during extension and pull off the surface of the sample during retraction.

It is most common to crack and destroy the tip when calibrating photodetector sensitivity when performing SFS measurements on a hard substrate (elastic modulus above 10 GPa). Unfortunately, it is even more common that the tip shape will not be exactly hemispherical after performing sensitivity, even with utmost care. It is quite difficult to accurately calibrate the photodetector without destroying the tip, especially when using ultrasharp tips with small radius of curvature. A good alternative in avoiding tip damage from sensitivity calibration is offered in a recent method developed involving thermal tuning to estimate sensitivity, without the need to perform force curves.[81] This is a little less of an issue for adhesion measurements because typically relatively soft cantilevers can be calibrated with minimal forces, but nonetheless tip shape is just as critical in this case. This problem is much less critical when microscopic colloidal probes are used, where the contact area is much larger.

After carefully engaging, the calibration force curves must be obtained extremely carefully. The scanner should be set to take individual curves as opposed to continuously taking curves. The trigger should be extremely small to avoid excessive deformation. That said, the trigger is directly dependent on the photodetector sensitivity. Therefore, initially one should assume a value slightly higher than typical sensitivity to avoid large forces in the first few curves. Typically, triggers should be set to 5–10 nm or less for relatively stiff surfaces and even below 1 nm for very stiff cantilevers. Relatively small ramp sizes should be selected to increase the number of data points in the contact region of the curve and to help prevent tip damage.

The number of performed force curves should be minimized; a few (5–10) repeatable measurements at given location is usually sufficient. The engagement and sensitivity measurement should be performed at least several times in different locations to ensure accuracy and eliminate site-specific deviations. It is common to destroy a tip or two in order to estimate the parameters to get force curves in a safe manner. It should be stated that much of these problems can be avoided by performing the sensitivity after the force curves are obtained, but there are some disadvantages to this approach, which are discussed in detail in the section on issues regarding the execution of these measurements.

2.2.2.3. Avoiding Surface Damage. To measure the linear elastic modulus it is imperative to avoid plastically deforming the sample surface. Trigger values should be set by keeping in mind the applied force, which ideally should not exceed a few nN. It is critically important that the sample should be imaged in tapping mode before and after (should be zoomed out prior to scanning) the force curves are obtained. If plastic deformation occurs it will appear in the zoomed-out image as an array of indentation marks. Furthermore, plastic deformation can often be recognized in the force curves as a leveled-off slope at a fairly uniform deflection and from hysteresis between approaching and retracting portions of force–distance curves.

2.2.2.4. Execution of Measurements. The order of execution that the elastic modulus measurements are performed is critically important.

A common procedure execution can be described by the following steps:

1. Clean silicon immediately before measurements as described in sensitivity calibration.
2. Warm scanner head for at least 15 min, depending on the system; always ensure that the head is warm before taking any SFS data.
3. Perform sensitivity calibration, verify linearity, and optimize photodiode signal.
4. Characterize tip shape and radius. Proceed if tip shape is hemispherical.
5. Estimate initial cantilever spring constant (e.g., by using manufacturing data).
6. Image sample surface at several locations and magnifications.
7. Perform force curves and examine deflection–penetration ratio to ensure that cantilever spring constant is appropriate (note that, without measuring sensitivity first, this is just a gross estimation).
8. Scan surface again in zoom-out mode to verify absence of indentation marks.
9. If appropriate, repeat the tip calibration and check the tip shape again.
10. If there is any change in the total photodetector sum, repeat the photodetector calibration.
11. Measure the exact value of cantilever spring constant.
12. Conduct data processing and analysis of the results.

An alternative to the execution listed above would be to perform the sensitivity at the end of the measurements, which prevents tip damage to great extent. But without knowing the sensitivity before the SFS measurements, the trigger and the deflection–penetration ratio can only be roughly estimated by doing sensitivity on a tip from the same box before the measurements and being careful to put the laser spot on the same part of the cantilever. As mentioned earlier, an alternative sensitivity calibration method developed by Higgins et al., which involves thermal tuning, can be used to avoid tip damage.[81]

The trigger, penetration–deflection ratio, and total penetration are very important and so by not knowing sensitivity one is essentially going at it blind, hoping for the best. So, there is a trade-off, because significant time can be wasted when inappropriate experimental conditions are used due to a lack of knowledge of the sensitivity. When the sensitivity is obtained after the measurements, data processing is required to apply the correct sensitivity. If the sensitivity is performed after the measurements to ensure tip preservation, then steps 1–3 should be moved and can replace step 9. It is important to note changes in the laser spot, typically observed as a change in the detector sum, because this is an indication that the sensitivity calibration changed over the course of the experiments and thus the measurements are void.

There are several other things to note when performing measurements, including that the scanner warming is not critical for scanners with a z-closed loop. The order of the cantilever spring constant calibration is not too critical, although often knowledge of the sensitivity is required depending on the calibration method, and one may damage the tip performing the tip-on-tip method of calibration. A second tip size calibration may be necessary in the case of a mistake leading to larger forces, if the sample is very stiff or if there is an indication of tip contamination. If the tip size noticeably changes in the course of probing, everything should be redone with a new probe.

2.2.2.5. Tip–Surface Contact Models for Elastic Modulus. Calculating elastic moduli from applied loading force and sample penetration data involves applying a model to account for the tip–surface contact area. Here, the most basic and common models are presented briefly, specifically the Hertzian model, Sneddon model, and Johnson-Kendal-Roberts. These models are inappropriate for materials with nonlinear elasticity, such as certain gels and biological materials. The reader is referred to several reviews for detailed information regarding nonlinear elastic contact models.[82,83] Typically, equations are derived from a quasi-static spring-on-spring model or force balance approach as expressed by

$$z_{defl}\, k = P(h) \tag{1}$$

where P is the applied force and h is the sample penetration as already defined.[84] Assuming a spherical tip, flat surface, and no plastic deformation, one can define an effective spring constant or stiffness for a material as:

$$k_M = \left(\frac{\partial P}{\partial h}\right) = 2r\frac{E}{1-\nu^2} \tag{2}$$

where r is the tip–surface contact radius, E is the material elastic modulus, and ν is the material Poisson's ratio.[85] Unfortunately, even after determining the tip radius, there is currently no known way to measure the contact radius at nanoscale in real time as the measurements are performed. Instead, contact mechanics models are used for fair estimation, which generally differ in the approaches on considering tip–surface interaction's contribution to the contact area.[62,63]

The most popular Hertzian contact mechanics model is applicable for small deformation and it assumes that the adhesion forces are zero and that at zero applied load the contact area is also zero, all of those being far from true in most SFS measurements. However, in the vast majority of practical cases these contributions can be ignored or proper corrections can be made. The force as a function of penetration depth described by the Hertzian model is

$$P = \frac{4}{3}R^{1/2}h^{3/2}E' \tag{3}$$

where R is the tip radius and E' is the composite modulus defined as

$$\frac{1}{E'} = \frac{3}{4}\left(\frac{1-\nu_S}{E_S} + \frac{1-\nu_T}{E_T}\right) \tag{4}$$

where the subscript S and the subscript T refer to sample- and tip-related variables, respectively. The modulus associated with the probe is generally assumed to be much larger than the elastic modulus of the surface, which is surely true for all polymeric surfaces. Therefore, a simplified equation for the elastic modulus based on the Hertzian approximation can be expressed as:

$$E = \frac{3}{4}\left(\frac{1-\nu^2}{R^{1/2}}\right)\left(\frac{dP}{d(h^{3/2})}\right) \tag{5}$$

When plotting the penetration raised to the 2/3 power versus the deflection (or the applied force) a straight line should result from data taken with a spherical tip and little to no surface–tip interaction. Poisson's ratio is usually taken as known bulk values typically ranges between 0.3–0.5 (about 0.5 for most of elastic materials/scenarios) are modest considering overall minor contribution in Eq. (5).

The Sneddon model is another popular model that can be utilized to describe tips with an elliptic paraboloid shape and for significant deformations. In this approach, the paraboloid function

$$Z = bX^2 \tag{6}$$

is utilized to describe the contact area as:

$$a = \sqrt{\frac{h}{2b}} \tag{7}$$

where R in Eq. (5) can be replaced with $1/(2b)$ to calculate the elastic modulus.

The Johnson-Kendal-Roberts (JKR) model includes an adhesive contribution, which can be expressed in terms of a reduced load, P_{JKR}. The elastic modulus from the JKR can be described by the modified Hertzian relationship between the load and the contact area as:

$$E = \frac{3}{4}\left(\frac{1-\nu^2}{R^{1/2}}\right)\left(\frac{dP_{JKR}}{d(h^{3/2})}\right) \tag{8}$$

where the reduced load, P_{JKR}, is defined as:

$$P_{JKR} = \frac{P_{Off}}{\sqrt{3}}\left(P_1^{3/2}\right) \tag{9}$$

where P_{Off} is the force associated with the snap-from portion of the force curve, line 5–6 in Figure 5, and P_1 is defined as:

$$P_1 = (3P_2 - 1)\left(\frac{1}{9}(P_2 + 1)\right)^{\frac{1}{3}} \tag{10}$$

where P_2 is defined as:

$$P_2 = \left(\frac{Z_{defl}}{Z_{adh}} + 1\right)^{\frac{1}{2}} \tag{11}$$

where Z_{adh} is the cantilever deflection associated with the snap-from, line 5–6 in Figure 5.

As mentioned earlier, there is a discrepancy regarding the initial deformation at snap in, or the zero contact point. This point is usually taken as either the snap-to point (the minimum deflection point in the extension curve) or the zero deflection point after the snap-to in the deflection curve, the imaginary intersection point between line 1–2 and line 3–4 in Figure 5. The initial penetration overestimates the modulus and as the penetration depth increases the measured modulus will steadily decrease to the "true value." If the total deformation well exceeds (two to three times) the initial contact penetration, the true value of the elastic modulus can be obtained anyway. This is a usual case for elastic materials where overall elastic deformation of 10–100 nm utilized for data analysis is much higher the initial deformation of 0.5–3 nm.

2.2.3. Examples of SFS Measurements. There are many different ways to utilize the elastic modulus and surface stiffness measurement capabilities of SFS. Choi et al. demonstrated the variation of the elastic modulus in periodic polymer structures fabricated by multi–laser beam interference lithography.[86] The variation in the elastic modulus of the SU8 microstructures was believed to be to due to the periodic variation in the cross-linking density resulting from the light intensity distribution. These measurements avoided effects of geometry by careful control of the probed depth. On the other hand, macroscopic deformation measurements (tensile test and peel test) were performed to reveal the ductile failure

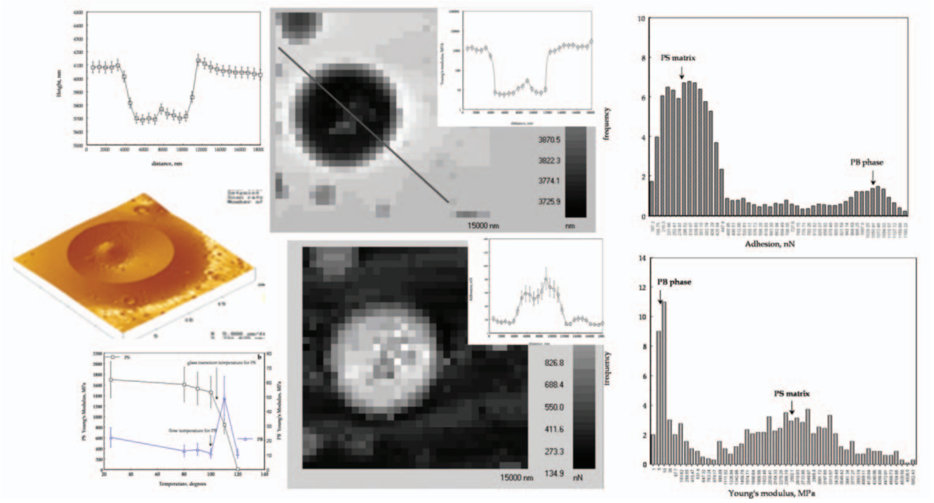

Figure 8. Rubber microphase inclusion in glassy polymer matrix for PS-PB blend (AFM topography slice, top, left) along with examples of force mapping (3-D topography, middle; topography, top; modulus, bottom) and surface histograms for adhesion (right, top) and modulus (right, bottom). Temperature variation of the elastic modulus for glassy and rubbery phases are presented as well (left, bottom). (Adapted from Tsukruk et al.[91] Copyright Elsevier.)

and necking of the thin nanoscale struts.[87,88] SFS measurements can also be very useful to probe phase transitions by performing measurements with varying probing frequencies and/or sample temperatures as demonstrated in several cases.[89,90]

For instance, we studied the surface distribution of the adhesive forces and elastic moduli for heterogeneous glassy–rubbery polymer films.[91] Micromechanical properties of polystyrene–polybutadiene (PS-PB) thin films were probed in the range of temperatures. We demonstrated that for heterogeneous films fabricated from polymer blends, the micromapping of surface properties can be obtained concurrently for glassy and rubber phases as well as across the interface with a lateral resolution better than 100 nm (Figure 8). Histograms of the surface distribution display two very distinctive maxima for both adhesive forces and the elastic moduli, which allows concurrent measurements of micromechanical properties of glassy and rubber phases. Glass transition temperature of glassy matrix and flow temperature of the rubber phase can be also detected by this technique by measuring the surface distribution of elastic modulus in a range of temperatures. Both temperatures (glassy and rubbery phases) derived from these mapping were demonstrated to be close to the known values (Figure 8).

The nanomechanical behavior of molecularly thick (8–10 nm) compliant polymeric layers with the nanodomain microstructure from grafted block copolymer, poly[styrene-b-(ethylene-co-butylene)-b-styrene] (SEBS or Kraton), was probed with micromechanical surface analysis based on scanning probe microscopy.[92] The micromapping with high lateral resolution (below 8 nm per pixel) revealed the bimodal character of the nanomechanical response with different elastic moduli shown by the rubber matrix and the glassy nanodomains (Figure 9). High-resolution probing showed virtually constant elastic response for the compliant layer compressed to 60% of its initial thickness followed by a sharp increase of the resistance when the tip reached within 3 nm from a stiff solid substrate.

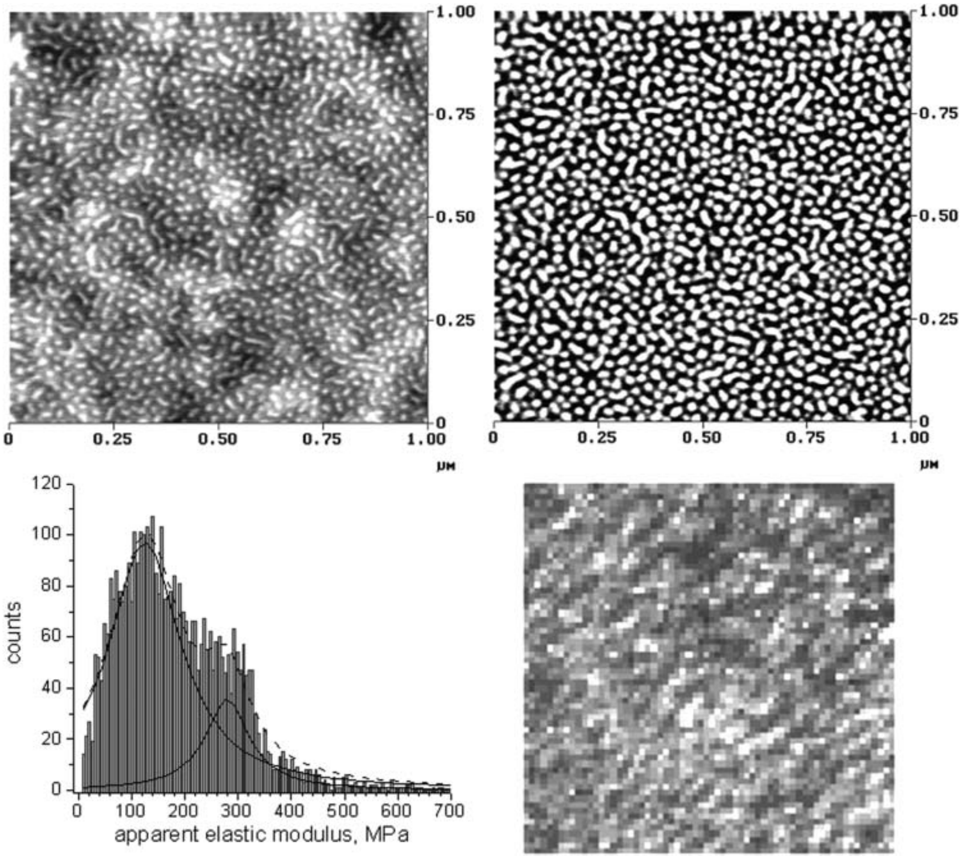

Figure 9. Top: AFM images (topography and phase of SEBS layer). Bottom: Surface distribution of apparent elastic moduli for the polymer layer collected with 64 × 64 resolution, size is 500 × 500 nm, lighter areas correspond to higher moduli along with histogram of the elastic modulus obtained from micromapping. (Adapted from Luzinov et al.[92] Copyright Elsevier.)

Application of the double-layer deformational model allowed the estimation of the actual elastic moduli of different nanophases within the grafted polymer monolayer: 7 ± 3 MPa for the rubber phase and 20 ± 7 MPa for the glassy domains (Figure 9). Relatively high elastic modulus of the rubber matrix is caused by a combination of chemical cross-linking/branching and spatial confinement within $<2R_g$ layer. On the other hand, the observed low modulus of the glassy nanodomains can be attributed to both low molar weight of PS blocks and the presence of rubber layers in the probed volume.

The approach developed for the microindentation of layered elastic solids was adapted to analyze SPM probing of ultrathin (1–100 nm thick) polymer films on a solid substrate.[93,94] The model for analyzing nanoindentation of layered solids was extended to construct two- and tristep graded functions with the transition zones accounting for a variable gradient between layers. This "graded" approach offered a transparent consideration of the gradient of the mechanical properties between layers (Figure 10).

By adapting this approach we considered polymer layers with elastic moduli ranging from 0.05 to 3000 MPa with different architecture in a solvated state and in a dry

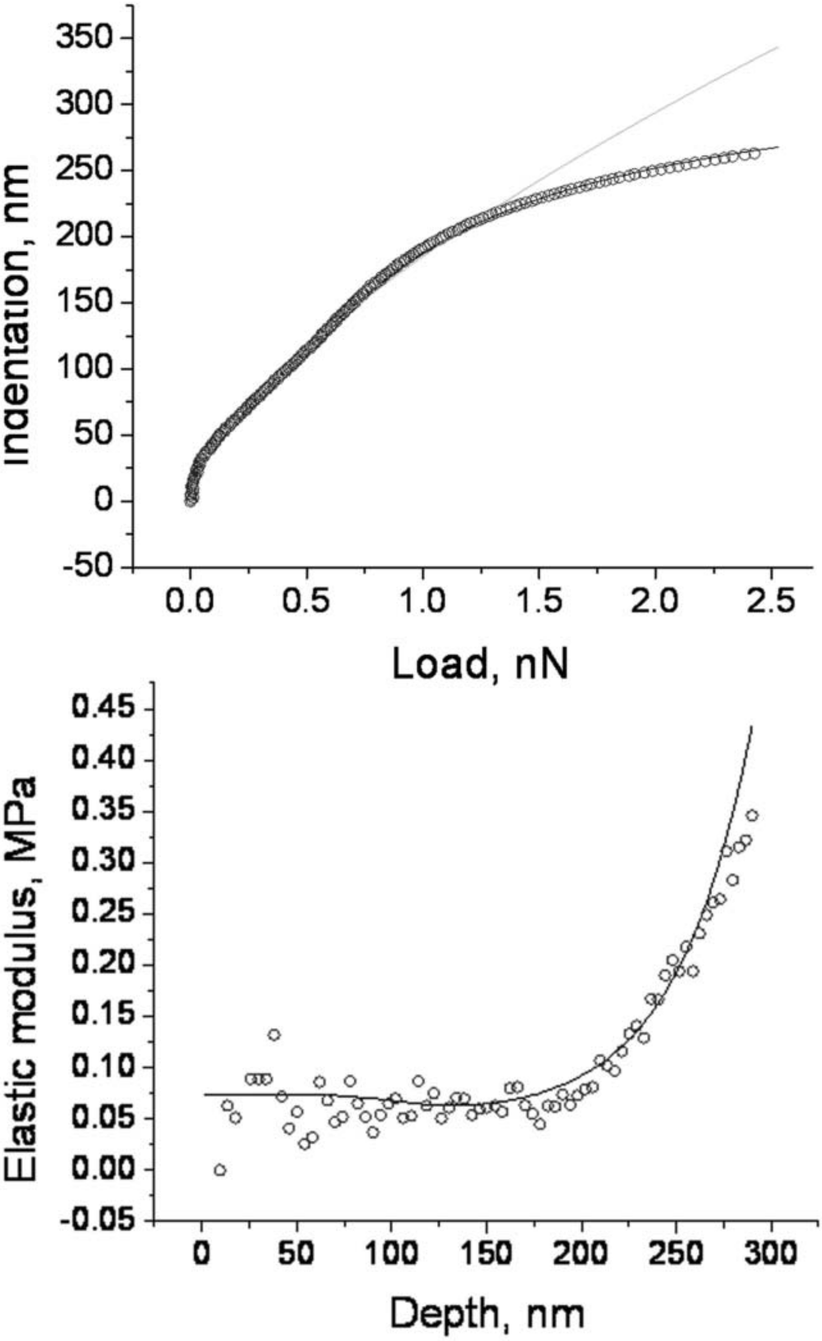

Figure 10. Top: Experimental loading curve (circles), fitting with the trilayered model (solid line, almost completely buried by experimental data points) and Hertzian model (dot line) for polymer brush in good solvent. Bottom: Experimental depth distribution of the elastic modulus for the polymer brush layer (circles) and the best fitting with the trilayered model (solid line) showing slight increase in the elastic modulus near the surface and sharp increase in proximity to a stiff substrate. (Adapted from Kovalev et al.[93] Copyright Materials Research Society.)

state, respectively.[93] The most sophisticated case of a trilayered polymer film with overall thickness of 20–50 nm and a combination of hard–soft–hard interlayers was also successfully treated within this approach. In all cases, a complex shape of corresponding loading curves and elastic modulus depth profiles obtained from experimental data were analyzed with the graded functions with nanomechanical parameters (elastic moduli and transition zone widths) close to independently determined microstructural parameters (thickness and composition of layers) of the layered materials.

The elastic properties of dendritic (hyperbranched) molecules with diameter below 3 nm have been probed with SFS, which allows for the micromapping of the surface stiffness and adhesion with nanoscale resolution.[95,96] To anchor dendritic molecules to hydroxyl terminal groups and reduce tip–molecule interactions, a modification of the silicon surface with an amine-terminated SAM and the AFM tips with methyl-terminated SAMs was used in this study. The nanomechanical response was analyzed in terms of sequential deformation of dendritic molecules and alkyl-silane monolayers (Figure 11). We observed much lower adhesion in the surface areas occupied by dendrimers as well as lower elastic modulus in these areas in comparison with the surrounding surface of SAM. This difference is caused by the reduced contact area between tip and 3-nm-diameter molecules and their high compliance in comparison with alkylsilane SAMs. Higher stiffness was also revealed for molecules within long-chain aggregates compared to individual molecules and small aggregates.

Though traditionally SFS is most commonly used to probe glassy and rubbery materials, it is also used to probe materials with elastic moduli in the range of Pa-KPa, including hydrogels and biological materials. SFS has proved to be an invaluable technique in probing biological materials and a number of significant results can be found in literature, but only a few examples will be presented here. Although overall methodology for probing biological and synthetic materials is based upon similar fundamentals, specific routines, data collection, and interpretation might be very different. The reader is referred to relevant reviews for use of AFM for biological applications.[97–100] Discussion of these differences is beyond the scope of this review.[62] We point out a few very recent results for highly compliant and viscoelastic biological materials such as dynamic AFM probing of articular cartilage with both traditional sharp AFM tip and colloidal probes by Stolz et al.,[101] mechanical probing of rat hippocampus and cortex areas as a function of aging by Elkin et al.,[102] or monitoring changes in brain tissue specimens after injuries with microindentation by Shafieian et al.[103] In a simple but robust study, Harmon et al. studied elastic modulus changes with temperature of photo-cross-linked poly-N-isopropylacrylamide swollen in water.[104] The network's modulus varied from 4.5 to 490 kPa over a 27°C range. The mechanical behavior with temperature was related to the degree of cross-linking and the polymer volume fraction.

Gelatin films have been studied by Braithwaite and Luckman and a complex relationship between elastic and viscous responses has been found for different separations of tip and substrate.[105] They concluded that careful analysis of these relationships could result in a separate calculation of loss and storage elastic moduli. Multi-element spring-dashpot models have been applied to analyzed force–distance curves. A quasilinear viscoelastic model was tested by Triphathy and Berger for SFS studies of agarose materials in order to derive full information on the viscoelastic behavior in a swollen state.[106]

Discher and coworkers used SPM to probe the elasticity of cell substrates and cell stiffness providing strong evidence that substrate stiffness significantly influences the cell lineage that stem cells express.[107] McConney et al. probed a signal filtering material under varying frequencies and related the frequency-dependent mechanical properties of the

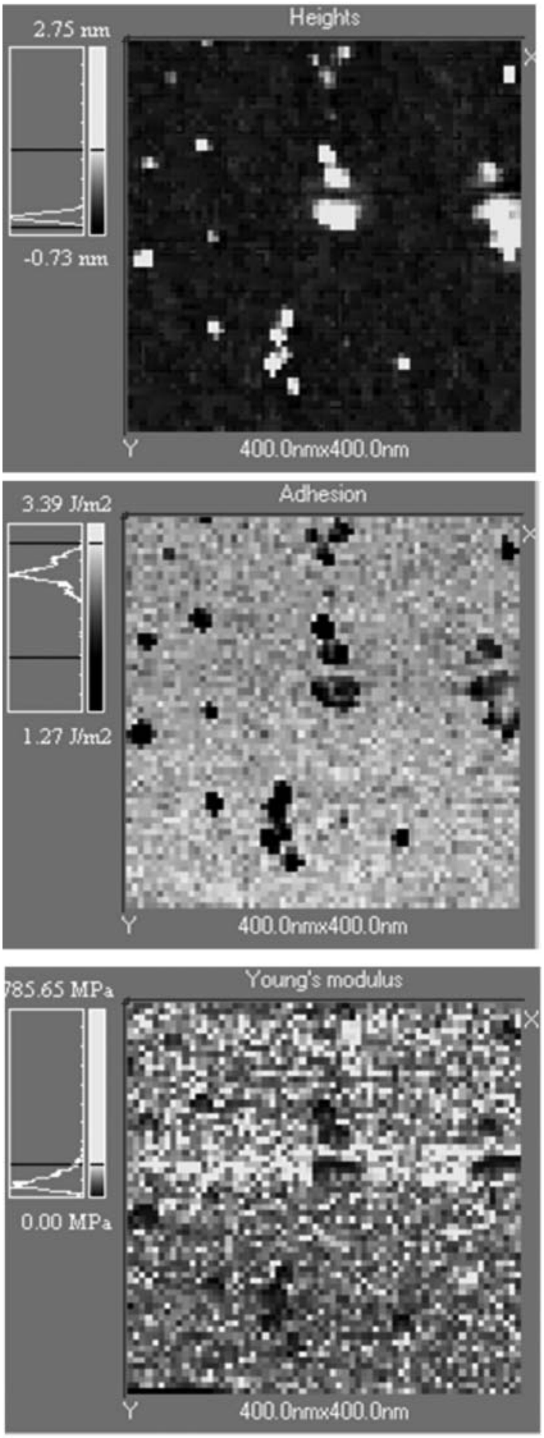

Figure 11. SFS micromapping of G3 molecular aggregates, 64 × 64 array, 400 × 400 nm area: topography (top) and concurrently obtained surface distribution of adhesive forces (middle) and elastic modulus (bottom). (Adapted from Shulha et al.[95] Copyright American Chemical Society.)

biological material to the viscous signal-filtering ability, much as those found in spider hairs.[108,109] The authors also studied biohydrogel cupulae of several different fish that are essential for underwater orientation of these species; these measurements helped guide the development of a bio-inspired material.[110] A particularly novel use of SFS elastic modulus measurements demonstrated by Yamada and coworkers involved measuring the elastic modulus of rabbit muscle.[111] The measurements found that the modulus tranverse to the muscle fiber changed from 11.5 in the relaxed state to 84.0 kPa in the contracted state.

2.2.4. Adhesion and Chemical force Spectroscopy. Quantifying adhesion from force spectroscopy can provide information regarding the intermolecular interactions and surface energies. Usually, precise measurements aimed at understanding specific chemical interactions involve the use of chemically modified tips in a mode of so-called chemical force spectroscopy. Chemical force spectroscopy is capable of providing rich information regarding chemical interactions with lateral resolution down to a single molecular group. A full discussion of chemical force spectroscopy and other associated techniques is beyond the scope of this review and the readers are referred elsewhere for more information.[112–116]

Adhesion force information is collected in the retraction portion of the force curve at the snap from region and usually pull-off forces are considered to be representative of true interactions, although some issues relevant to instability in tip behavior should be always considered. Often this adhesion data is a combination of several forces, which can include contributions from capillary forces, electrostatic forces, van der Waals forces, hydrogen bonding, ionic bonding, and covalent bonds. Capillary forces tend to dominate adhesive forces in ambient air, which are commonly on the order of 1–100 nN.[115,117–119] Although capillary forces can be used to gauge hydrophobic/hydrophilic forces and thereby provide contrast, most adhesion measurements are aimed at obtaining chemical interaction information, where capillary forces are considered an undesirable interference. Therefore, in order to avoid overwhelming contribution from capillary forces, SFS measurements are performed under dry nitrogen or immersed in liquid.

It should be stressed that much like elastic modulus measurements, there are errors associated with calculating the work of adhesion and surface free energies and care should be taken in both the measurements and data analysis. In this case the Hertzian model is inappropriate, and instead JKR and Derjaguin-Müller-Toporov (DMT) contact models are commonly employed. Under the JKR theory, the work of adhesion is defined as:

$$W_{SMT} = \frac{3}{2}\pi\left(\frac{R}{P_{ad}}\right) \tag{12}$$

where R is the tip radius and P_{ad} is the force required to separate the tip from the sample surface. The DMT theory results in similar relationship with 3/2 coefficient replaced with 2. Both models have shown good agreement with experimental data despite mechanical instability of the cantilevers during pulling-off event and are more applicable to different limiting cases (materials with different balance of compliances and adhesion), as discussed elsewhere.[84]

Measurements on various surfaces performed in various solvents are well reported. Figure 12A presents force curves in ethanol for SAMs with different tip and surface functionalities.[120] Measurements immersed in aqueous environments have led to more specialized measurements, namely, measuring the pK of surfaces, which can be powerful for investigating surface confinement effects of the ionizability of functional groups on

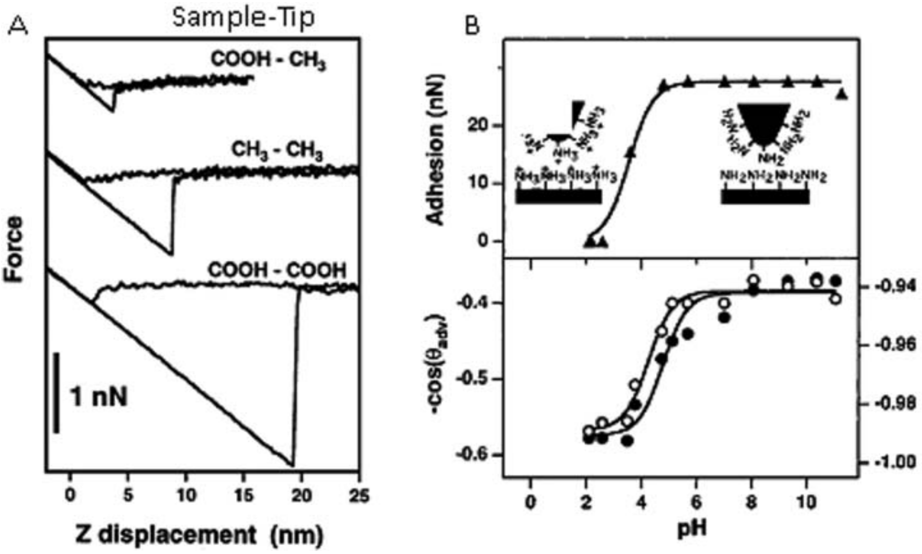

Figure 12. Adhesion measurements are highly effected by surface chemistry, solvent, and probe chemistry (A) Top: a force–titration curve; Bottom: a corresponding contact angle titration curve. This figure demonstrates the capability of force spectroscopy to measure interfacial energy. (B) Force–distance curves taken in different solvents and with different tip functionalities. (Obtained from Noy et al.[120] with permission from the American Chemical Society.)

the surface. In fact, there are significant differences in the dissociation constants from macromolecular surfaces compared to monomers in solution, which can be attributed to a variety of factors, including decreased available degrees of freedom associated with bonding/immobilization, the effect of the dielectric permittivity from adjacent functional groups, and the electrostatic free energy of the substrate.[112,121] These differences are usually measured by quantifying the surface energy through contact angle measurements taken at different pHs.

Similar measurements can be performed by monitoring adhesion forces between functionalized tips and surfaces with solution pH, through the so-called force–titration measurements introduced by Lieber et al.[122] Figure 12B shows a plot comparing results from force titrations and contact angle titrations. Measurements involving surface that are incapable of dissociation show no effect from pH changes. A force–titration approach has the ability to map the surface energies on the nanoscale and associate any energetic contrast with nanoscale features.[123] It should be mentioned that in order to probe unknown surface *pK*s, it is important to use tips functionalized with hydrophilic groups that are incapable of changing ionization with pH.[112] Force–titration measurements demonstrate the important role that the surrounding fluid plays in localized adhesion measurements with SFS. Variants of this technique can also be used to study the interactions between macromolecules in different chemical environments. Jiang et al. explored the interaction of hydrophobic and hydrophilic polyamines with polyethylene oxide (PEO) at various solution pHs, which has key implications for PEO's applications as a biocompatible material and anti-biofouling material.[124] Surprisingly, this work indicated that polyallylamine, a hydrophobic polyion, can have favorable adhesion to PEO in an aqueous environment.

There are many different ways to apply the capabilities of adhesion measurements and chemical force microscopy toward polymeric materials. A major area of interest in composite material development is the interaction of functional micro-/nanofillers with polymer matrices. A novel use of force spectroscopy has been in quantifying these interactions. For example, Barber et al. studied the interaction of carbon nanotubes and polyethylene-butene with the use of probes with nanotubes attached to the tip.[125] This was accomplished by repeatedly heating the polymer matrix above the glass transition temperature, pushing the nanotubes into the polymer, and cooling and then pulling the nanotubes back out of the polymer, as is shown in Figure 13A.

The interactions between individual functional groups and individual groups on freshly prepared carbon nanotubes has also been studied by LeMieux et al. with functionalized tips in fluidic environment achieving single molecular group interactions conditions for a variety of important functional groups (Figures 13B and C). Intermolecular interaction histograms obtained in this study were shown to follow proper theoretical predictions based upon the variation of the electronic state for different gaps. These results can be used to

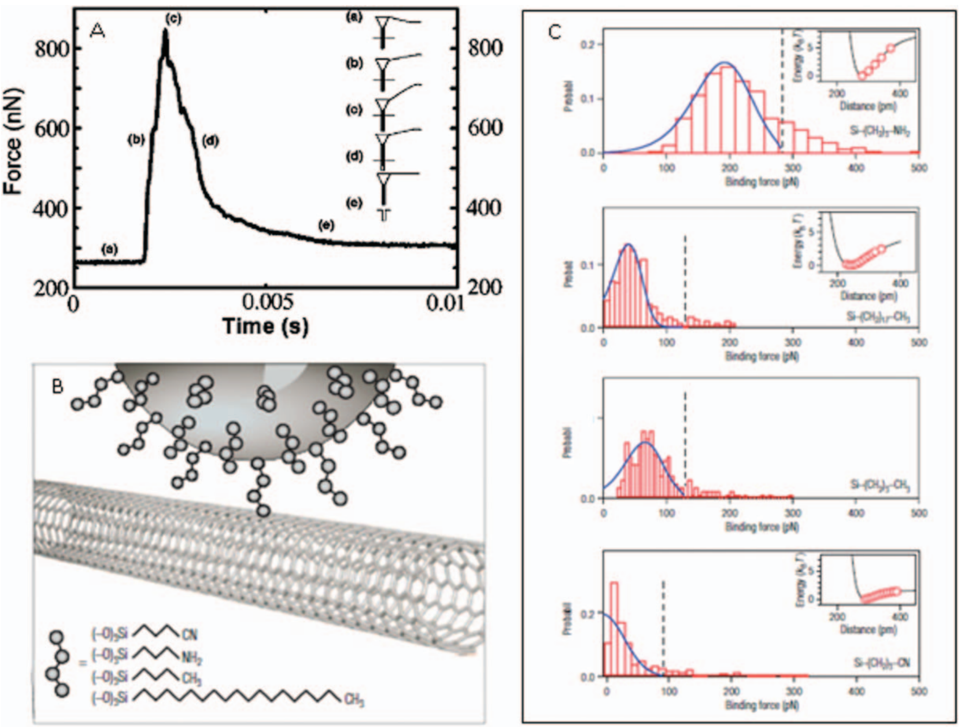

Figure 13. Studies using force spectroscopy to measure the interaction energy between soft matter and carbon nanotubes. (A) A graph showing the force to pull a carbon nanotube out of a polymer matrix. The inset is a schematic explaining the testing approach and the various regions of the graph. (B) A schematic indicating the testing method of another study involving measuring the single molecule interactions with carbon nanotubes. (C) The resulting data provide the binding force histogram of the different molecules with the wall of single-wall carbon nanotubes. ((A) obtained from Barber et al.[125] with permission from The American Institute of Physics; (B) and (C) adapted from Friddle et al.[126] Copyright Nature Publishing Group.)

better design carbon nanotube–polymer interfacial chemistry and can be considered for understanding of surface defects in carbon nanotubes.[126]

2.3. *Pulsed-Force Microscopy*

Pulsed-force microscopy (PFM) is a popular method used to map topography, relative stiffness, adhesion, and electrostatic properties at about 1 ms per a pixel, about 1,000 times faster than conventional force spectroscopy. Since the advent of PFM by Marti and coworkers, the popularity of this method is gaining momentum, especially since it has become commercially available.[127]

Simplistically stated, PFM is essentially dynamic force-curve mapping. PFM typically involves driving a z-piezoelement with amplitude from 10 to 500 nm at 100 Hz to 5 kHz, orders of magnitude less than the cantilever resonance frequency, thereby obtaining force curves on the millisecond timescale.[128] The z-piezoelement is driven with a sinusoidal profile, as opposed to the triangular wave that drives typical force curves. A typical PFM force–distance curve can be seen in Figure 14A, with the piezoelement driving signal plotted as the dashed line.[129]

PFM uses minimized forces, which avoids plastic deformation with ease. Furthermore, PFM measures and maps adhesion force directly. This technique acquires the same information as static force spectroscopy mapping, but the sampling is much faster. The height, stiffness, and adhesion measurements come from a peak-trough picking routine, which is used to quickly process the data, thereby providing images. The system acts under a constant force mode, like static force spectroscopy mapping, and therefore sample stiffness can slightly affect the height data. Softer domains would appear to be depressed compared to stiffer domains on a soft sample. The high sampling rate that the stiffness and adhesion forces are probed have a significant effect on the apparent behavior of the material due to time–temperature superposition effects.

A study comparing adhesion data from SFS and PFM for poly-4-methyl-1-pentene under varying temperature highlights differences between the methods.[128] The SFS and the PFM data show an expected increase in the absolute adhesion force with temperature, but the absolute adhesion force drops much less in the PFM data than the data from SFS as shown in Figures 14B and C. The difference is due to an apparent shift in the glass transition caused by the much higher probing frequency of PFM. Another interesting effect of the fast probing times is that amorphous regions can counterintuitively appear more sticky than crystalline domains, which have a higher surface energy, because the amorphous chains are much more mobile.

Therefore, it should be quite apparent that SFS and PFM are highly complementary techniques. Between SFS and PFM, one could probe polymers at frequencies from 0.01 Hz to 5 kHz probing frequency range, where conventional SFS ranges from 0.01 Hz up to frequencies approaching 100 Hz and PFM ranges from 100 Hz up to 5 kHz.

2.4. *Friction Force Microscopy*

Friction force microscopy (FFM) is an AFM-based technique used to characterize the tribological properties of surfaces.[130] Common measurements with these modes involve relating frictional forces to applied normal forces (so-called loading curves). These measurements involve the use of an AFM in contact mode controlling normal loads and monitoring the lateral cantilever deflection (torsion) signal, as shown in Figure 15, left. FFM imaging can

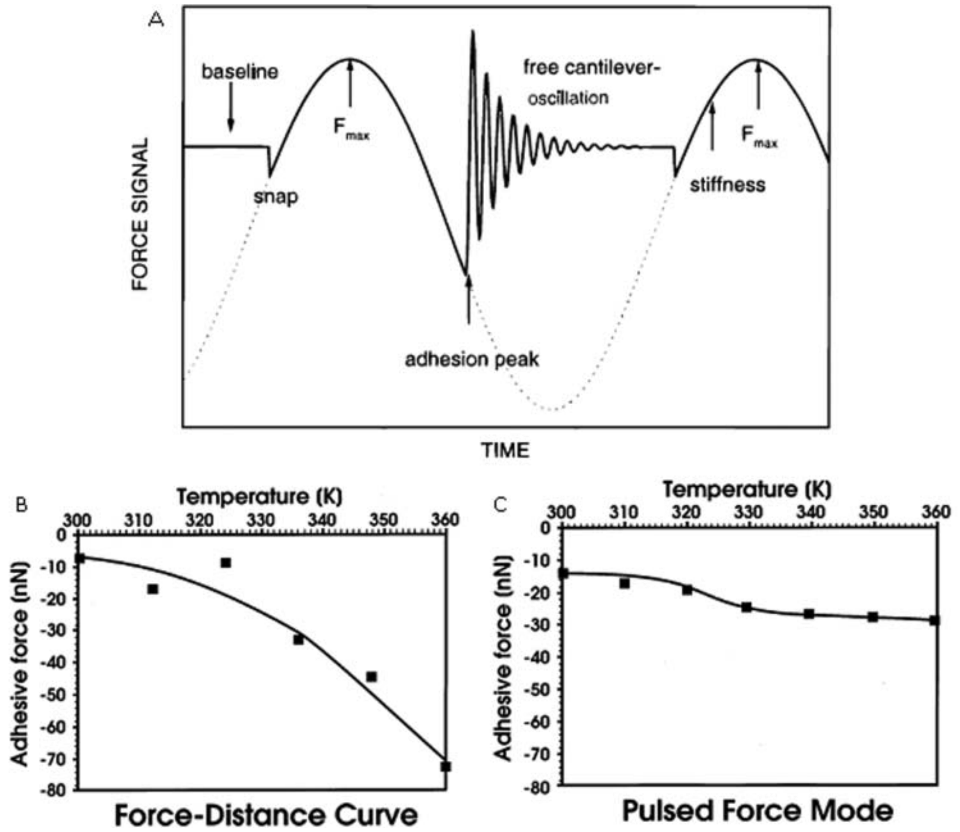

Figure 14. (A) A schematic showing the resulting force data from pulsed force microscopy. The dotted line shows the relative force modulation voltage. The arrows indicate the points picked to acquire the baseline, maximum applied force, and adhesion. (B) Adhesion vs. temperature from SFS and (C) from PFS of poly(4-methyl-1-pentene) ($T_g = 303$ K). ((A) obtained from Krotil et al.[129] with permission from Wiley-Blackwell; (B) and (C) obtained from Marti et al.[128] with permission from Elsevier.)

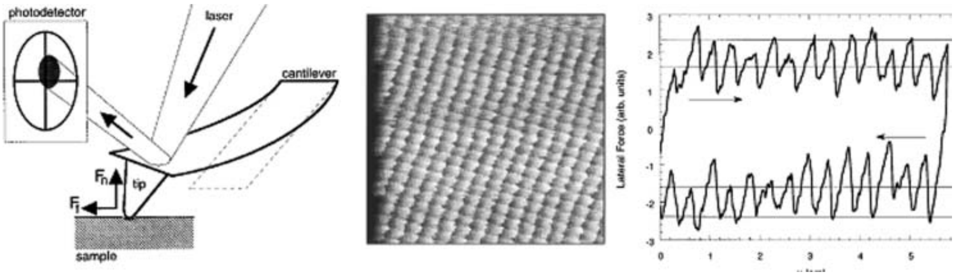

Figure 15. Right, a schematic showing the lateral and normal forces applied in FFM and the resulting laser spot deflection in the photodetector. Center, a 6 × 6 nm friction force image of KF (001) imaged in ultra high vaccuum. Left, a friction loop, indicating the average force level for each direction and the clear hysteresis between the directions. (Obtained from Carpick and Salmeron[130] with permission from the American Chemical Society.)

be as simple as scanning a surface in contact mode and using the lateral signal to produce a friction force image. The probe is scanned back and forth across a sample surface, generating so-called friction loops, which are the base for lateral force microscopy (LFM), another term for FFM (see Figure 15, center).

Therefore, each back-and-forth cycle produces a "friction loop" curve as shown in Figure 15, right. The average friction force is quantified as half of the difference between the average friction force of each direction of the friction loop. A sample region is scanned under several different normal loads, thus producing a friction force vs. normal load curve. Usually measurements are performed on homogenous areas of a sample with smooth surface. Friction force images are often obtained for heterogeneous samples and the friction force contrast is associated with adhesive properties of components with common spikes between different areas recognized as "geometrical" friction artifact.[131]

Typically, measurements involve conventional silicon and silicon nitride probes, but diamond-coated probes are becoming popular for friction measurements because of the reduced wear associated with these probes. It is also possible to obtain chemical-related information from friction force images, especially when obtained with chemically functionalized probes. This can be done by simply obtaining a friction force image on a chemically heterogeneous sample.[114] Friction at nanoscale is still far from well understood, but FFM has indeed provided an avenue for a deeper understanding. A notable example of the impact FFM has had on the understanding of friction was work performed by Carpick and coworkers.[132] FFM (or LFM) is useful for polymeric studies involving reducing material wear, enhancing lubrication, stiction in microelectromechanical systems (MEMS), and other nanotribological phenomena.[16,133,134] FFM can be sensitive to chemical information, especially when functionalized tips are used, providing information on shearing behavior of surface layer, friction coefficients, wearing dynamics, and velocity-dependent shearing.

Application of FFM to SAMs, adsorbed molecular layers, and Langmuir-Blodgett (LB) monolayers from amphiphilic molecules have been widely exploited to elucidate their morphology and applicability as molecular lubricants with a variety of regular and extremely sharp tips.[15,133] An example of FFM imaging of heterogeneous LB film from amphiphilic stearic acid presented in Figure 16 clearly demonstrates extremely low localized friction in selected areas coated with organic monolayer.[135] Concurrently, extremely high friction is observed on bare silicon surface areas on the same image. FFM has also proved to be an invaluable technique for analyzing frictional properties of biological materials, such as cartilage. A notable example by Ortiz and coworkers involved the application of FFM in analyzing cartilage aggrecan under varying ionic strengths and with varying length scales.[136] They found that at low ionic strength the lateral force did not vary with the lateral displacement rate, but at physiological ionic strengths the macromolecules' frictional force significantly increased with the lateral displacement rate. This work provided molecular-scale insight into the deformation behavior of cartilage macromolecules. Vancso and coworkers performed FFM with varying tip radii over different temperature and wide frequency range (1–10^7 Hz) on polymethyl methacrylate to study the effects of surfaces on molecular mobility and free volume.[137] This detailed study resulted in a master curve that was used to quantify the activation energy associated with the α relaxation mode and the sub-Tg β relaxation modes. The results showed a significant decrease in activation energies associated with the surface as compared to bulk values. This study in effect put to rest the controversy related to the effect that surfaces have on molecular mobility of glassy materials.

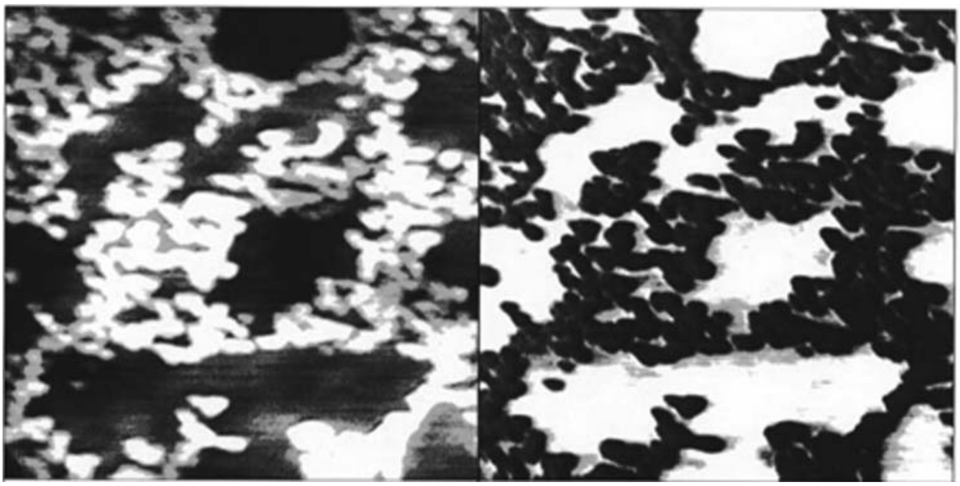

Figure 16. Topography (left) and friction (right) for incomplete Langmuir-Blodgett monolayer of stearic acid (1 × 1 μm) showing high friction on silicon (bright areas) and very low friction on LB monolayer (dark areas). (Adapted from Tsukruk et al.[135] Copyright American Chemical Society.)

3. Thermal Characterization of Polymers

3.1. Approaches

Studying the local thermal properties of materials is of fundamental importance in understanding a variety of phenomena, including photon–phonon interactions, electron–phonon interactions, molecular motion, and various phase transitions.[138] Although various thermal characterization techniques based on SPM have been developed, this review will focus on methods based on AFM techniques combined with the electrical resistance thermometry, which is applicable to polymer materials and is relatively well developed. This includes scanning thermal microscopy (SThM) imaging of thermal conductivity and other local thermal analysis (L-TA) techniques. The term *micro-* or *nano-thermal* analysis (micro-/nano-TA) encompasses a variety of techniques involving characterizing localized material properties on a temperature controlled sample.

Control over the temperature of a sample is provided by the use of a thermally active, electrically resistive probe (thermal probe) and/or a variable temperature microscope stage (temperature stage). If the latter is being used, practically any type of probe normally available for AFM may be mounted in the microscope. A thermal probe may function as a thermometer as well as a heat source. This enables a different type of micro-/nano-TA to be carried out, in which heat is applied to the sample from an external energy source (infrared radiation, for example) and the probe is used to sense the resulting change in temperature of the material. This approach enables spectroscopy to be carried out with a spatial resolution that is, in theory, better than the diffraction limit.

Initially, Wollaston wire probes (loops) were the most common. These thermal probes were developed by Dinwiddie et al.[139] and first used by Balk et al.[140] and Hammiche et al.[141] A diagram of the construction details of this probe is shown in Figure 17, top.[142] The Wollaston probe with loop diameter of several tens of a micrometer is a relatively massive structure compared with most inert probes used in other forms of AFM. The Wollaston probe, whose high and variable spring constant (5 to 20 N/m) and complexity

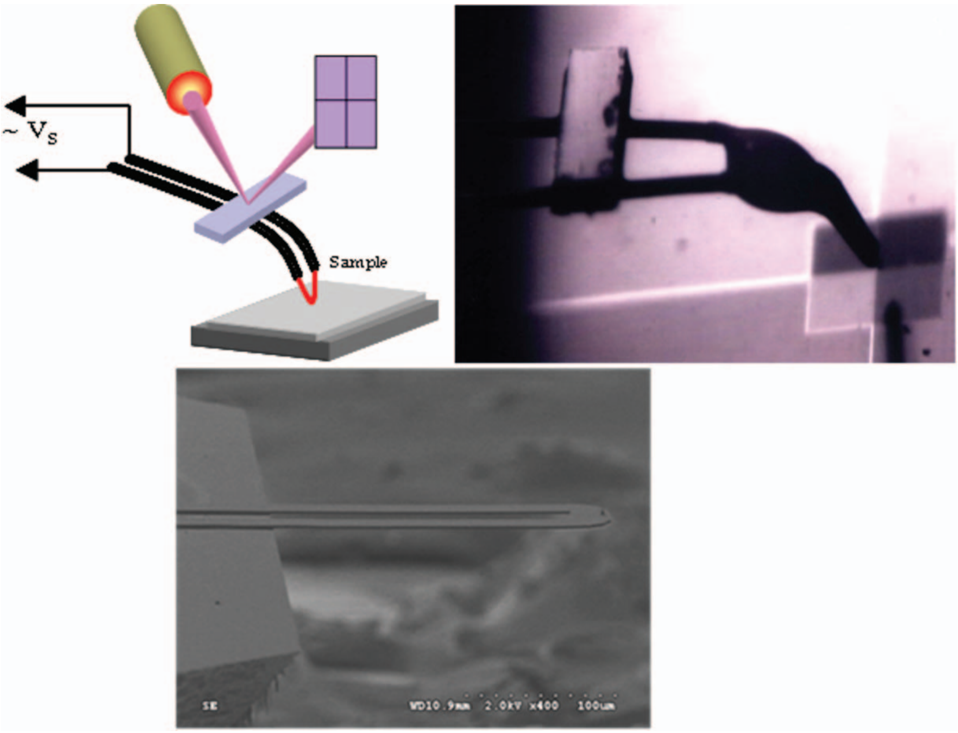

Figure 17. Top: A schematic (left) of a Wollaston resistive probe and corresponding micrograph (right). Bottom: A scanning electron micrograph of higher resolution thermal probes. (Top images were obtained from Gorbunov et al.[153] Copyright Sage Publications; bottom image is reproduced with permission from Anasys Instruments, Inc.)

render it unsuitable for all but the contact mode. These probes routinely perform with spatial and thermospatial resolution on the submicrometer, although nanometer resolution is occasionally reported.[140,141,143–147] Temperature distribution in the contact area of the thermal tip and polymer surface is relatively sharp under fast probing even with large thermal tip (Figure 18).[148]

Some of the best results for robust routine local thermal analysis with high spatial resolution comes from probes based on the approach adopted by King et al.[149] The spatial resolution of these probes is the same as conventional AFM tips. Unfortunately, though these probes are capable of imaging topography at nanometer scale, these probes are not suitable for high-resolution thermal imaging. The heated area is on the top of the inverted pyramidal tip; this means that the resistive element that is sensitive to temperature is relatively large, of the order of 10 μm (Figure 17, bottom). The effect of this combination is that the heater serves very well to heat the tip, but the thermal resistance thermometer function is impaired.

Microfabricated bowtie probes are probes where the metal conducting layer has a bowtie shape at the tip so that electrical resistance is located at the narrow middle area.[147] Elongated rectangular discontinuities in the coating are detected in thermal images down to a width of 200 nm but only when lying parallel to the raster direction. The resolution perpendicular to this direction is shown to be roughly a factor of two poorer. Nonetheless,

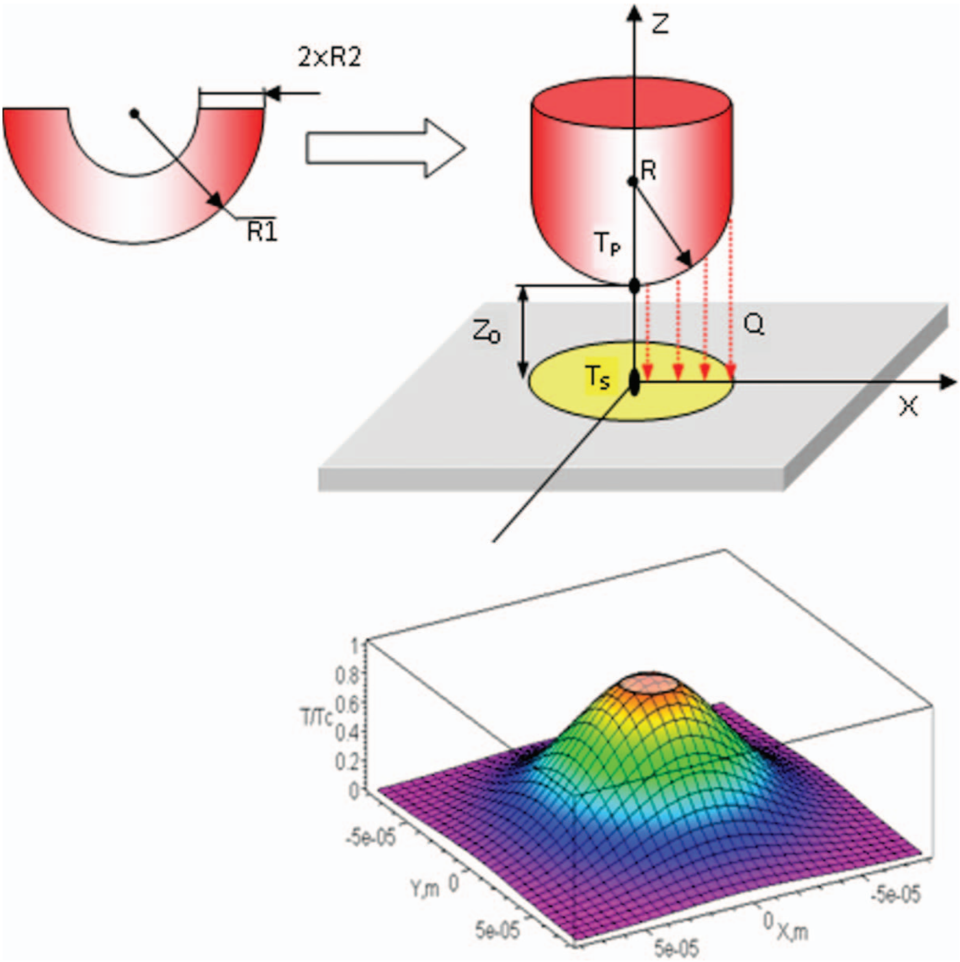

Figure 18. Modeling of temperature distribution in the contact area of thermal tip. (Obtained from Tsukruk et al.[151] Copyright Elsevier.)

electrical-resistance thermometry probes are an active area of development and future developments will surely lead to enhanced thermal resolution.

Quantitative thermal conductivities measurements can be obtained from both SThM and local-TA measurements as well.[142,150] It is important that the temperature within the thermal contact is virtually homogeneous ($<3\%$ of variation for all materials) and the temperature in the center of the heated zone, T_c, can be used for the estimation of the average temperature.[151] Also taking into consideration that the thermal probing of a surface can easily satisfy a quasi-stationary case for heat flow from the thermal probe to a surface, the heat transfer can be described by a quasi-stationary equation to analyze the dynamics of the heat dissipation as well.[150]

SThM enables the acquisition of images of the surface of a sample constructed from spatial contrast in one or more thermal properties of the material.[147] The most common form of SThM is constant temperature mode, and SThM is used here to refer to this mode. In constant-temperature SThM, the thermal probe is held at a fixed temperature by means of a thermal feedback loop as it is raster-scanned across the surface of the sample. The AFM force-feedback mechanism holds it at a constant contact force. The power supplied to the thermometry probe to maintain it at the selected temperature is recorded and used to construct the "thermal conductivity image."[145] Areas of relatively high thermal conductivity will result in more power being supplied to the thermal probe than neighboring areas with lower conductivity.

As with many SPM-based techniques, interpreting thermal images acquired with SThM is complicated by surface topography effects caused by variations in the contact area. For Wollaston wire probes, surface roughness above 30 nm can significantly affect quantifying thermal conductivity.[152] Even with a thermally homogeneous material, the surface topography gives rise to thermal image contrast. It is also possible for topographical effects to mask or interfere with contrast of thermal images of multiphase materials. Because of this effect a careful visual comparison of the topographic and thermal images must be made to determine how closely the location, size, and shape of features in one image are reflected in the other. This problem is greatly reduced when a flat sample surface can be prepared by sectioning or polishing.

3.2. Local Thermal Analysis

Local thermal analysis refers to a localized thermal measurement, much like force–distance curves are localized mechanical measurements. Typically, L-TA measurements do not involve mapping. These measurements are performed by contacting the surface with probe under a set force and then running a thermal measurement.[141,143,153] After the tip is exerting a predetermined downward threshold force (i.e., cantilever deflection), a temperature ramp is applied to the sample via the probe. This is usually a linear heating program or linear heating followed by linear cooling. Heating and cooling cycles may be set at different rates. Essentially, two signals are acquired simultaneously, the vertical deflection of the probe and the power required to ramp the probe temperature providing information on thermomechanical properties.

Indeed, the measurement of probe deflection with temperature is the micro (or local) analogue of thermomechanical analysis used on bulk samples (micro-/nano-TMA, L-TMA). Similarly, the measurement of probe power consumption is the micro-analogue of differential thermal analysis (micro-DTA, L-DTA). Both of these techniques have been used extensively in the study of thermal transitions in polymers and other materials.[148,154]

Once the probe is in contact with the surface and the temperature program is initiated, the force-feedback mechanism is disabled and the fixed end of the cantilever remains at a constant height throughout the experiment. Therefore, these experiments are not constant force experiments. Thermal expansion typically results in a steady increase of the cantilever deflection (thus in an increase in applied force) and an increase in the sample penetration. For a material that undergoes no thermal transitions over the temperature range of the experiment, the probe deflection with temperature will be essentially linear and upwards as the sample beneath the probe heats and expands.

Heating a sample to a phase transition results in the softening of the sample material, measured by both a dramatic increase in the sample penetration (decrease in cantilever deflection) and an increase in power required to sustain the probe temperature. Figure 19 is a graph of the resulting data from a typical micro-TMA and micro-DTA experiments on polyethylene terephthalate (PET) surface, demonstrating how well-defined glass transition and melting phenomena reveal themselves in L-TA data during the heating cycle.

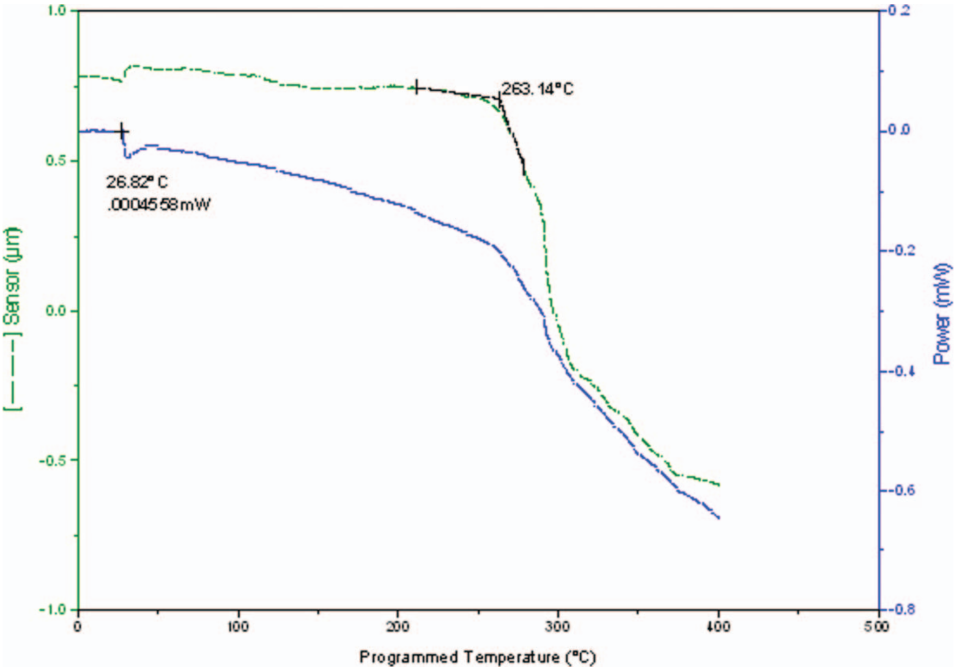

Figure 19. A typical micro-TMA and micro DSC curve for poly(ethylene terephthalate). (Adapted from Gorbunov et al.[154] Copyright Sage Publications.)

The heating of the probe element itself causes some movement of the cantilever, but for the relatively massive Wollaston wire thermal probe this effect should be minimal. Providing that a baseline subtraction procedure is carried out (acquired from a run with the probe in free air), the rate of power consumption of the probe over the duration of the same experiment on a sample should remain constant. When heating polymer through phase transitions (a glass transition, cold crystallization, curing, melting, or degradation), the response of the micro-TA signals can be quite rich and distinctive, as illustrated in Figure 19.[151] This behavior shows typical micro-DTA and micro-TMA results for a crystallizable but initially mostly amorphous polymer. There is a large indentation at the softening temperature (around the glass transition temperature) and then a further indentation at the melting temperature. It is important to note that, the DTA signal is not sensitive to enthalpies like differential scanning calorimetry (DSC).

During data analysis and interpretation it is important to note that L-TA is highly dependent on changes in the contact area; therefore, it cannot be known just from these data. This is a disadvantage of the micro-/nano-TA approach compared to conventional calorimetry. However, the glass transition and melting events are clearly detected. Furthermore, there are still many advantages to L-TA, including mapping DTA and TMA at sub-nanometer scale. L-TA can also be used to analyze ultrathin films. L-TA can be also used to study differences between surface and bulk properties through the use of suitable sectioning techniques.[155]

AC heating can be applied to SThM and such approach can also be applied to L-TA experiments. AC heating may be applied to the thermal probe. This produces a fixed temperature modulation in the range of ±1 to ±10°C, although it is usually confined between ±2 and ±5°C. This may be seen as analogous to the development by Reading and coworkers[156] of modulated temperature differential scanning calorimetry (MTDSC).

In micro-/nano-TA the response of the sample to the modulated and underlying heat flows can be separated using a deconvolution program. The modulated regime is sensitive to the reversible changes in the heat capacity of the material, associated with molecular vibrations, and the latter detects changes due to kinetically controlled processes that are unable to reverse at the temperature and the rate of the modulation. An obvious advantage of this technique is its ability to characterize heterogeneous samples in which different types of transitions occur over the same temperature range. Theoretically, the use of AC heating offers similar advantages to those of modulated-temperature DSC over conventional DSC. It has been shown that the AC signals may be particularly sensitive to thermal transitions that produce a relatively large change in heat capacity for a small heat input.[157]

3.2.1. Thermal Probe Calibrations. In order to measure the temperature of local transitions, a temperature–resistivity calibration of the thermal probe must first be carried out. The subject of temperature calibration has been addressed comprehensively by Blaine et al.[158] and by Meyers et al.[159] This process typically involves measuring the resistivity of the tip at the melting transition of known calibration samples. These calibration samples should be over several hundred nanometers thick to avoid substrate contributions. Furthermore, the calibration sample's thermal conductivity should be considerably less than the probe material thermal conductivity. The L-TA technique acquires two signals (L-TMA and L-DTA), of which one should be used to indicate the transition for calibration samples. Presently, it seems better to use the L-TMA signal because this has a higher signal-to-noise ratio.

The temperature calibration should be carried out on two or more substances whose melting temperature (T_m) is well known from the literature. For this purpose, it is often more convenient to use polymer films whose melting point has previously been measured using DSC or another technique. This does make the assumption that the enthalpies measured in DSC experiments can be considered to mirror their mechanical analogues (i.e., softening). There is now a reasonable body of data in the literature that allows one to conclude that this assumption is, broadly speaking, appropriate. When using DSC data as the point of comparison there is the question of which characteristic temperature on the DSC curve should be chosen as the one corresponding to the penetration temperature.

Several researchers have suggested using the extrapolated onset temperature of melting, but it is known that the leading edge of melting endotherms of polymers is not straight, so the determination of the "extrapolated onset temperature of melting" is subjective.[158–160] Nonetheless, a good correlation between bulk and local measurements has been demonstrated, with the variation of the transition onset of ±3°C.

3.2.2. L-TA of Ultrathin Polymer Films. Analysis of the ultrathin polymeric films on a high-conductivity substrate is a significant challenge. The huge difference in the thermal conductivity of a polymeric film and a substrate results in heat dissipation mostly to the substrate through the tested film. In this case, L-TMA and L-DTA measurement procedures should be significantly modified.[151] To account for the substrate, one can engage a separate reference probe on an identical substrate using a microscopic manipulator on a separate microstage under a stereo microscope. The two thermal probes should ideally have similar thermal characteristics and be independently tested prior to their selection to balance heat dissipation. With the modified measurement setup, the thermal sensitivity of the thermal

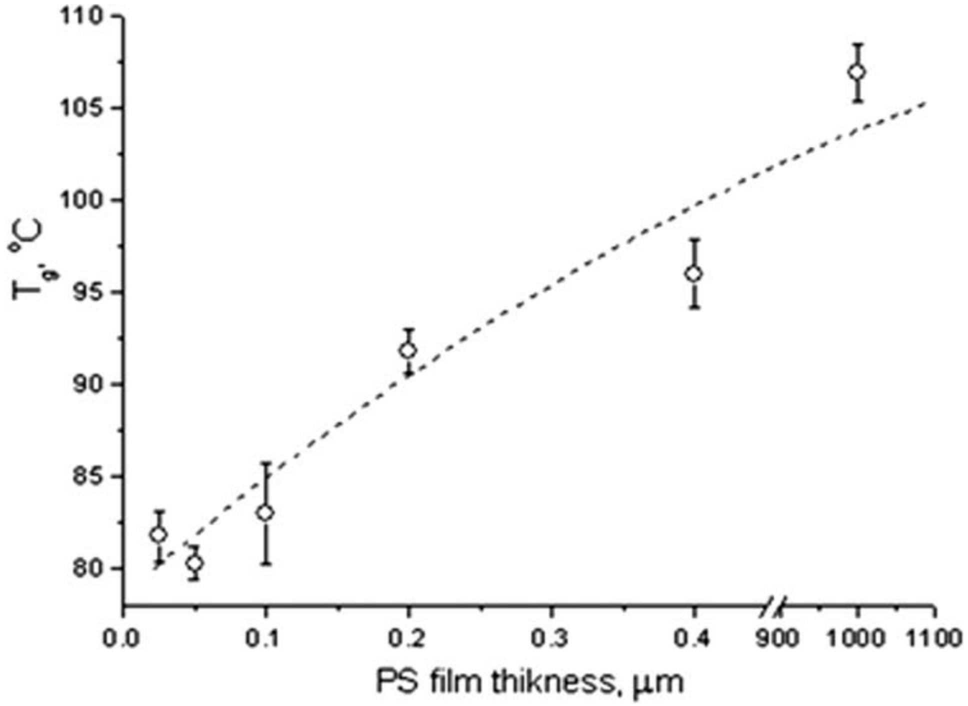

Figure 20. Glass transition of polystyrene vs. film thickness. (Adapted from Gorbunov et al.[154] Copyright Sage Publications.)

probe increases dramatically, thus allowing detection of minute heat dissipation variations (<1 μW) associated with the polymer film itself.

The experimental data shown in Figure 20 indicate that the glass transition temperature decreases when the film thickness is less than 400 nm (compare this data with results for bulk PS film [1 μm thick] in Figure 20).[154] For the thinnest film presented in this plot, the glass transition temperature decreases by 20°C from its bulk value. These results follow general trends observed for ultrathin polymeric films deposited on solid substrates with weak film–substrate interactions. These results can also be explained because of enhanced chain mobility associated with the free surface.[161,162] This data demonstrates the sensitivity of the present micro-/nano-TA design to probe nanometer-thick polymer films.

L-TA has also been used to characterize photodegradation and other phenomena that cause chain scission by studying changes in the glass transition after exposure to polymer degrading processes.[163] It is interesting to note that force and heating rate have minimal effects on the melting temperature, but both force and heating rate have a significant effect on the glass transition temperature.

4. Electrical/Magnetic Characterization of Polymer Composites

4.1. Kelvin Probe Force Microscopy/Electrostatic Force Microscopy

Kelvin probe force microscopy (KPFM) and its simpler analogue electrostatic force microscopy (EFM) enable the spatial mapping of the work function and the surface potential distribution with a lateral resolution of a few nanometers and a potential resolution of a few mV. Work function (Φ) is defined as the minimum energy required to remove an electron from the electronic ground state in a material.[164] It is known that the work function (Φ) is a sensitive indicator of surface conditions and is affected by adsorbed layers, surface charging, surface imperfections, and surface and bulk contaminations.

Though macroscopic Kelvin probes for measuring the average work function for relatively large surfaces are known for a long time, KPFM was first demonstrated in 1987 using optical heterodyne detection to track the frequency changes in a vibrating AFM cantilever resulting from the normal electric field components of surface charges and potentials. In KPFM a conductive tip scans over the surface, interacting electrostatically with the surface under investigation. The potential of the tip to that of the surface is matched using an electronic feedback. When the potential of the tip exactly equals that of the material, electrostatic interaction between the tip and the sample is nullified. The voltage applied to nullify the electrostatic interaction is the local measure of the work function or more directly the contact potential difference between the tip and the surface. If the work function of the tip is known, a quantitative two-dimensional map of the surface work function can be constructed from the applied DC feedback signal. The KPFM technique is performed the noncontact mode and does not involve the injection of any charges into the sample as in conductive AFM.

Electrostatic force microscopy, on the other hand, is much simpler in that the technique does not involve in an electronic feedback. EFM is typically operated in lift mode, as previously described. An oscillating (at the resonance frequency) conductive tip biased at fixed DC voltage scans over the surface electrostatically interacting with the surface. EFM measurements are performed in two different modes: DC mode and AC mode. In the DC mode, a conductive tip oscillated near the resonance frequency (noncontact mode) with fixed DC bias (V_{tip}) scans over the surface at fixed height (few tens of nanometers) above the surface of the sample.

The tip electrostatically interacts with the sample and the changing electrostatic force with the vertical separation distance, which causes a shift in the resonance frequency and the phase ($\Delta\varphi$) of the cantilever given by

$$\Delta\varphi \propto (d^2C/dz^2)(V_{tip} + \phi - V_S)^2 \tag{13}$$

where Vs is the voltage within the sample, Φ is the work function difference between the tip and sample, V_{tip} is the tip voltage, and C is the tip sample capacitance. The observed phase shift is thus proportional to the square of the DC voltage difference between the tip and the sample. Thus, mapping the frequency or the phase shift as a function of the tip voltage pixel by pixel, or by calibrating the phase/frequency response of the cantilever as a function of bias and maintaining a constant value of V_{tip}, EFM can be employed to measure potential profiles with the high resolution.

KPFM has been employed for the investigation of organic solar cells comprised of poly-[2-(3,7-dimethyloctyloxy)-5-methyloxy]-para-phenylene-vinylene/1-(3-methoxycarbonyl) propyl-1-phenyl [6,6]C61 (MDMO-PPV/PCBM) blends, identifying a barrier for electron transmission from the electron-rich PCBM nanoclusters to the extracting cathode.[165] Figure 21 shows the topography and the KPFM mapping (under light illumination) of MDMO-PPV and PCBM blended film that was spin cast from chlorobenzene and toluene. The topography images clearly reveal that in the case of the films deposited from chlorobenzene, polymer nanospheres are distributed almost evenly throughout the bulk of the film, whereas a skin layer, incorporating polymer nanospheres, surrounds the big PCBM

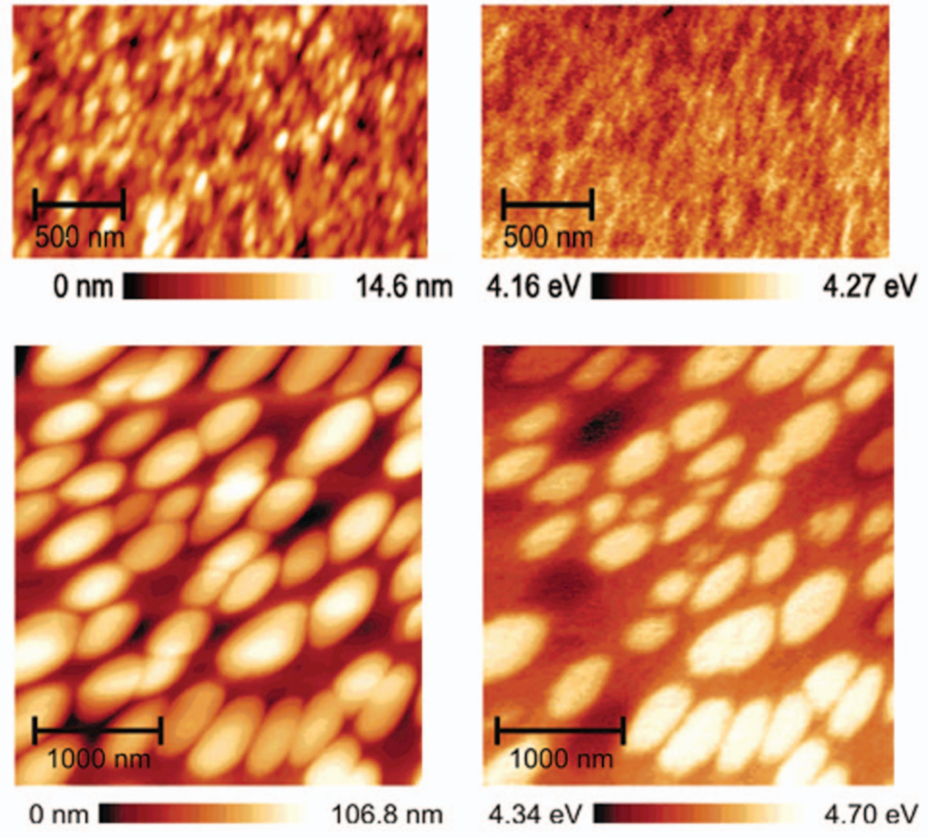

Figure 21. AFM and simultaneous KPFM images of the topography and work function of toluene-cast blend film of MDMO-PPV/PCBM with a mass ratio of 1:4, measured in the dark and under 442-nm laser illumination. (Obtained from Hoppe et al.[165] with permission from the American Chemical Society.)

clusters in toluene cast films. Apart from the dramatic difference in the morphology of the blend, the variation of the work function on the surface is much larger in the case of films deposited from toluene (0.1 eV) compared to that deposited from chlorobenzene (0.2 eV).

In a related study, Sirringhaus and coworkers have employed KPFM to map the surface potential and the photoinduced surface photovoltage and correlate this with the topography of the polyfluorene blend–based photovoltaic devices.[166] The results clearly suggest that an optimization of appropriate size of phase separation percolation of both the electron and hole transporting phases with their respective electrodes are highly essential for improving the efficiency of energy harvesting.

One of the significant issues with KPFM is that the experimentally obtained potential profiles do not generally reflect the true profile in the device due to complex coupling between the tip and the sample.[167] In the initial stages, it was believed that the tip–sample separation and tip radius are limiting factors of the resolution attained in KPFM measurements.[168–172] However, by combining experimental and finite element analysis, Charrier et al. have quantitatively shown that the potential profiles obtained by scanning Kelvin probe microscopy do not purely reflect the electrostatic potential under the tip apex but

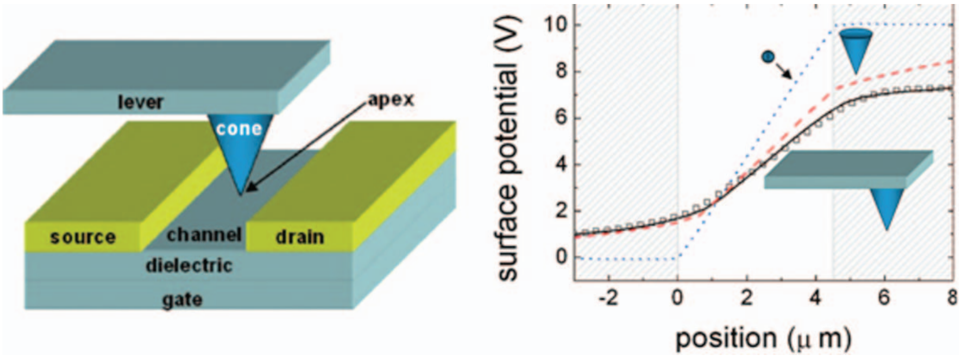

Figure 22. (a) Schematic showing the microcantilever orthogonal to the channel of the field effect transistor (FET) device. (b) Experimental potential profile with the lever orthogonal to the channel (squares) and modeling for a full 3D tip (solid black line) containing the apex, cone, and lever. The dashed line shows the simulation for a probe consisting only of the cone and apex, the dotted line for a probe consisting of only an apex. (Obtained from Charrier et al.[173] with permission from the American Chemical Society.)

are strongly affected by the electrostatic coupling between the entire probe and the entire device, even for small tip–sample separations.[173]

Figure 22A shows the experimental potential profile in the geometry shown in Figure 22B and three different modeling curves. The solid line is calculated for the full 3D probe consisting of the apex, cone, and lever. Calculations for a probe consisting of the cone + apex (dashed line) and only a single apex (dotted line) are also shown. It can be observed that removing the lever and leaving only the apex + cone, the full potential difference at the electrodes becomes 20% higher. Removing the cone and leaving the apex results in further deviation from the experimentally observed potential profile, clearly underscoring the importance of taking the entire probe and device geometry into account for reliable quantitative potential profiles.

4.2. *Conductive Atomic Force Microscopy*

Conductive atomic force microscopy (c-AFM) enables the simultaneous mapping of the topographical and electrical conductivity of the sample using a conductive AFM tip. This technique involves using the electrically conducting tip as one electrode and a conductive substrate or a metal electrode on the surface of the sample as second electrode. The measurement can be performed by either by applying a constant voltage between the tip and the metal electrode, with simultaneous recording images that can be used as a measure of the local conductivity, or collecting local I-V curves by sweeping the voltage between the tip and the other electrode, which can be mapped. In a different kind of measurement, I-Z curves can be obtained by holding the voltage constant while the *Z*-piezoelement is moved perpendicular to the sample surface, thereby changing the tip–surface contact area to determine the force where the conductivity saturates. This force is then used to image the conductivity in constant force.

Conductive AFM can be operated in two different configurations, namely, horizontal and vertical.[174–176] Vertical and horizontal modes are similar in that they both use a conductive AFM tip as an electrode, but the modes differ in the substrate electrode configuration. In the horizontal mode, the material under investigation is deposited on an insulting surface and is directly connected to an electrode. On the other hand, in the vertical configuration, the material is deposited on a conductive surface that acts a second electrode. Typically, c-AFM measurements are performed in the contact mode. However, this mode of operation results in the damage of soft polymeric and biological (e.g., DNA) samples. To avoid the potential damage of the sample surface, some groups have adapted an alternate approach that involves in acquiring the topography using a dynamic method such as tapping mode followed by point contact I-V measurements at predefined regions.[177]

c-AFM has been extensively employed to probe the morphology, conductivity, and carrier mobility of polymer thin-film devices.[178–182] One of the extensively studied system is the PEDOT:PSS blend commonly employed as a interface layer between the anode (ITO) and the organic semiconductor layer in various optoelectronic devices. A vertical c-AFM configuration was applied to study the effect of processing conditions (such as annealing, PSS content, solvent treatment) on the vertical charge transport of PEDOT:PSS.[183] Though the topography images do not show any significant change with annealing, from the conductive maps it was observed that most of the current passes through the film surface via small conductive hot spots in a relatively insulating matrix.

Figure 23 shows the topography and the c-AFM images of PEDOT:PSS film annealed at 140°C for different periods of time. The increase in macroscopic conductivity observed following the annealing of PEDOT:PSS films results from an increase in both the number of the conductive hot spots and current carrying capacity of the PEDOT domains observed on the film surface.

Apart from obtaining simultaneous topography and conductive maps, vertical configuration of c-AFM has been extensively employed to obtain current density voltage curves (J-V curves), which in turn were used to extract local hole mobilities, using space charge limited current (SCLC) model.[180,184] Carrier mobility is extracted by fitting the J-V data to

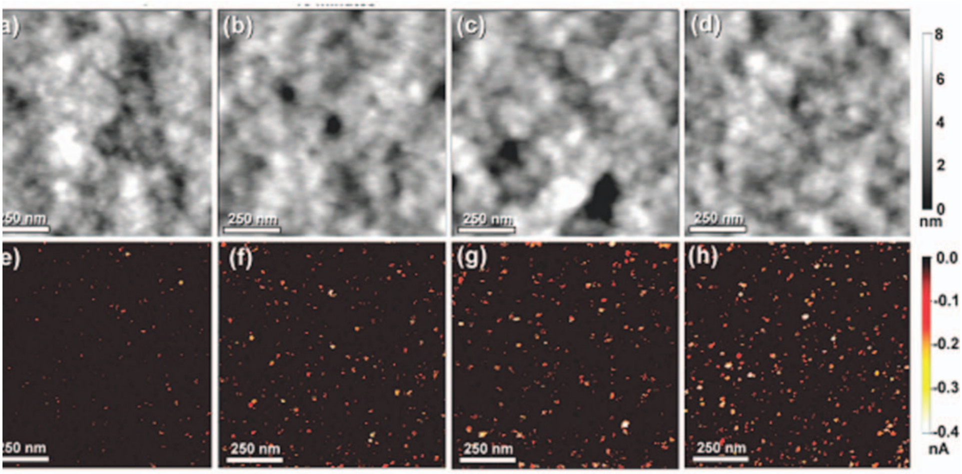

Figure 23. 1 μm^2 area AFM topography and c-AFM images of the PEDOT:PSS films annealed at 140°C: (a and e) 0 min, (b and f) 10 min, (c and g) 30 min, (d and h) 100 min. The topography (top row) exhibits very little change through the course of annealing, whereas the c-AFM images (bottom row) clearly show that the number of conductive pathways (bright spots) increase as function of the annealing time. (Obtained from Pingree et al.[183] with permission from the American Chemical Society.)

the Mott-Gurney law.

$$J = \frac{9}{8}\varepsilon\varepsilon_0\mu\frac{V^2}{L^3} \tag{14}$$

where J is the current density, ε is the relative dielectric constant of the active layer, ε_0 is the permittivity of free space, μ is the charge carrier mobility, V is the applied voltage, and L is the thickness of the device. However, the technique usually results in carrier mobilities higher compared to that observed in planar electrode configuration as the current spreads out under the AFM tip, enabling a larger space charge limited current density than is expected in the plane-parallel case as shown in Figure 24.

Ginger et al. have recently demonstrated that the primary cause of this observation is the fundamental difference in geometry between the two configurations, namely, planar electrodes and the vertical c-AFM.[185] Conventional Mott-Gurney law is not applicable for c-AFM measurements because SCLC measurements performed in this geometry deviate from the $J \propto L^{-3}$ dependence. Taking the tip sample geometry into account and using finite

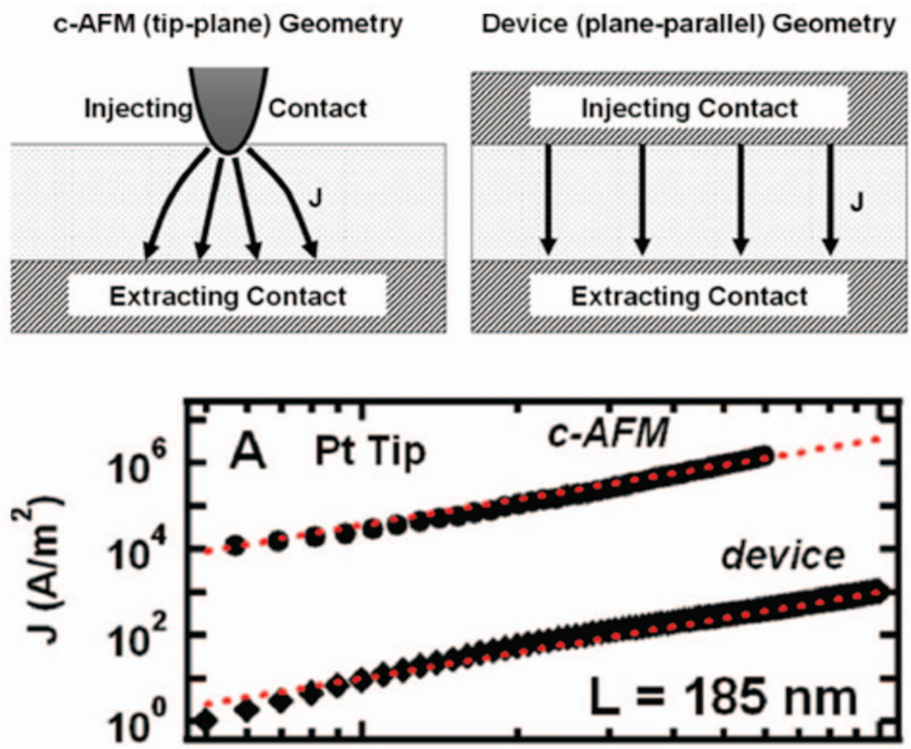

Figure 24. Top: Schematics showing the geometry of the c-AFM and planar macroscopic device measurement respective geometry. Current spreading laterally beneath the AFM tip results in a larger space charge limited current density than is expected in the plane-parallel case. Bottom: J-V curves measured using c-AFM (circles) and macroscopic devices (diamonds) on P3HT showing the apparently higher current density in C-AFM measurements. The grey dotted line shows the fit using classical Mott-Gurney law to each of the curves to extract the mobility. c-AFM measurement was made using a 50-nm-diameter platinum-coated tip. (Obtained from Reid et al.[185] with permission from the American Chemical Society.)

element analysis (FEA) simulations they have suggested a semi-empirical equation for the current density as

$$J = \alpha \varepsilon \varepsilon_0 \mu_0 e^{0.89\gamma (V/L)^{1/2}} \frac{V^2}{L^3} \delta \left(\frac{L}{D} \right)^{1.6\pm0.1} \tag{15}$$

which is valid for common tip diameters and sample thicknesses, using a scaling factor based on the ratio of tip diameter, D, to sample thickness, L. This scaling factor enables the extraction of quantitative values of charge carrier mobility from J-V curves collected by c-AFM for samples.

4.3. Magnetic Force Microscopy

Magnetic force microscopy (MFM) operates in the noncontact mode in which a tip coated with a ferromagnetic material (such as Ni, Co, Fe) detects the stray magnetostatic field of the magnetic dipoles of the sample. Because the magnetic interactions are long range (similar to the electrostatic interactions), the magnetic imaging is performed in lift mode with a set distance between the probe and surface of typically 20–50 nm. In MFM, during the second line scan the cantilever deflection is monitored and used to create the MFM image. MFM has been widely employed to probe magnetic recording media and imaging and magnetization of Co, Ni, and iron magnetic nanodots.[186–190] MFM has also been employed to image and estimate the magnetic moment of magnetotactic bacteria.[191] MFM has been employed to study the self-assembly of polyethylene glycol (PEG) and polystyrene-coated Fe_2O_3 nanospheres (magnetic nanospheres) under an external magnetic field.[192]

Sun et al. have described the polymer-mediated assembly of FePt nanoparticles using polyvinylpyrrolidone (PVP) and polyethyleneimine (PEI) polymers.[193] The assembly process involved the exchange of oleic acid/oleyl amine around the magnetic nanoparticles with a functional polymer that is previously deposited on a substrate. Figure 25 shows the

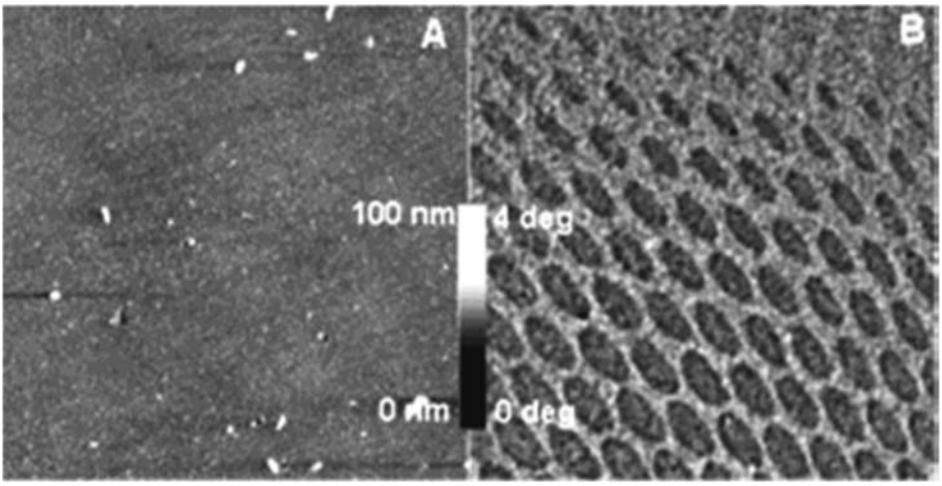

Figure 25. (a) AFM topography and (b) MFM image of a three-layer 4-nm Fe_{58}-Pt_{42} nanoparticle assembly annealed at 530°C. Whereas the AFM reveals the smooth surface topography of the assembly, the MFM image reveals the assembled particles. (Obtained from Sun et al.[193] with permission from the American Chemical Society.)

topography and the corresponding MFM image of a three-layer 4-nm $Fe_{58}Pt_{42}$ assembly treated with a pulsed laser under a perpendicular magnetic field (2.5 kOe). The AFM image shows that the smooth FePt nanoparticle assembly is intact after the laser treatment. The dark spots in MFM image indicate the magnetization pointing to the out of the particle assembly plane.

MFM has also been used for mapping the dispersion of carbon nanotubes in a polymer matrix.[194] From the MFM phase images, the carbon nanotubes were often found as agglomerates throughout the film. Furthermore, MFM also clearly revealed individual nanotube bundles and areas with high localization of nanotubes, which could not be observed in topographic images. The contrast between the nanotubes and the background was strongly dependent on the distance between the tip and the surface (lift height) with lift heights greater than 15 nm exhibiting diminished contrast.

5. Conclusions

This review summarized characterization techniques for soft matter that are based on close proximity probes. Mechanical, thermal, electrical, and magnetic characterization techniques were also presented. The review included a discussion of techniques, calibration procedures, and common pitfalls regarding force spectroscopy measurements and the characterization of elastic modulus and adhesion forces. Examples presented here are not comprehensive but rather selected to demonstrate the most important capabilities of the presented techniques and their applicability to polymeric materials.

Key examples of the method are presented to communicate the capabilities and impact that probe-based characterization techniques have had on the mechanical, thermal, magnetic, and electrical characterization of polymeric and composite materials. Main attention is paid on how measurements are conducted from practical viewpoint, how data should be processed, and several examples of corresponding recent results from application of a particular operation mode are briefly presented and discussed.

Acknowledgements

The authors thank S. L. Youth for technical assistance and the following agencies for continuous support in SPM studies of soft materials in the SEMA lab: NSF-DMR, NSF-CMMI, NSF-CBET, AFOSR, AFRL, ARO, DARPA, and DOE.

References

1. Binnig, G.; Rohrer, H. “Scanning tunneling microscopy,” *Helvetica Physica Acta*, **1982**, *55*, 726–735.
2. Binnig, G.; Rohrer, H.; Gerber, C.; Weibel, E. “Tunneling through a controllable vacuum gap,” *Applied Physics Letters*, **1982**, *40*, 178–180.
3. Binnig, G.; Rohrer, H.; Gerber, C.; Weibel, E. “Surface studies by scanning tunneling microscopy,” *Physical Review Letters*, **1982**, *49*, 57–61.
4. Gerber, C.; Lang, H.P. “How the doors to the nanoworld were opened,” *Nature Nanotechnology*, **2006**, *1*, 3–5.
5. Binning, G.; Rohrer, H. “Scanning tunneling microscopy—from birth to adolescence,” *Reviews of Modern Physics*, **1987**, *59*, 615–625.
6. Magonov, S. N.; Whangbo, M.-H. Surface Analysis with STM and AFM: Experimental and Theoretical Aspects of Image Analysis; VCH: New York, 1996.
7. Binning, G.; Quate, C. F.; Gerber, C. H. “Atomic force microscope,” *Physical Review Letters*, **1986**, *56*, 930–933.

8. Singamaneni, S.; LeMieux, M. C.; Lang, H. P.; Gerber, C.; Lam, Y.; Zauscher, S.; Datskos, P. G.; Lavrik, N. V.; Jiang, H.; Naik, R. R.; Bunning, T. J.; Tsukruk, V. V. “Bimaterial microcantilevers as a hybrid sensing platform,” *Advanced Materials*, **2008**, *20*, 653–680.
9. Raiteri, R.; Nelles, G.; Butt, H.-J.; Knoll, W.; Skladal, P. “Sensing of biological substances based on the bending of microfabricated cantilevers,” *Sensors and Actuators B: Chemical*, **1999**, *61*, 213–217.
10. Lang, H. P.; Berger, R.; Andreoli, C.; Brugger, J.; Despont, M.; Vettiger, P.; Gerber, C.; Gimzewski, J. K.; Ramseyer, J.-P.; Meyer, E.; Güntherodt, H.-J. “Sequential position readout from arrays of micromechanical cantilever sensors,” *Applied Physics Letters*, **1998**, *72*, 383–385.
11. Dutta, P.; Chapman, P.; Datskos, P. G.; Sepaniak, M. J. “Characterization of ligand-functionalized microcantilevers for metal ion sensing,” *Analytical Chemistry*, **2005**, *77*, 6601–6608.
12. Fritz, J.; Baller, M. J.; Lang, H.-P.; Rothuizen, H.; Vettiger, P.; Meyer, E.; Güntherodt, H.-J.; Gerber, C.; Gimzewski, J. K. “Translating biomolecular recognition into nano-mechanics,” *Science*, **2000**, *288*, 316–318.
13. Singamaneni, S.; McConney, M. E.; LeMieux, M. C.; Jiang, H.; Enlow, J. O.; Bunning, T. J.; Naik, R. R.; Tsukruk, V. V. “Polymer-silicon flexible structures for fast chemical vapor detection,” *Advanced Materials*, **2007**, *19*, 4248–4255.
14. Tsukruk, V. V.; Reneker, D. H. “Scanning probe microscopy of polymeric and organic molecular films: from self-assembled monolayers to composite multilayers,” *Polymer*, **1995**, *36*, 1791–1808.
15. Tsukruk, V. V.; Bliznyuk, V. N.; Hazel, J.; Visser, D.; Everson, M. P. “Organic molecular films under shear forces: Fluid and solid langmuir monolayers,” *Langmuir*, **1996**, *12*, 4840–4849.
16. Bliznyuk, V. N.; Everson, M. P.; Tsukruk, V. V. “Nanotribological properties of organic boundary lubricants: Langmuir films versus self-assembled monolayers,” *Journal of Tribology*, **1998**, *120*, 489–495.
17. García, R.; Pérez, R. “Dynamic atomic force microscopy methods,” *Surface Science Reports*, **2002**, *47*, 197–301.
18. Sheiko, S. S. “Imaging of Polymers Using Scanning Force Microscopy: From Superstructures to Individual Molecules”, in *New Developments in Polymer Analytics II, Advances in Polymer Science Vol. 151*; Schmidt, M., Ed.; Springer-Verlag: Berlin, 2000; 61–174.
19. Martin, Y.; Williams, C. C.; Wickramasinghe, H. K. “Atomic force microscope—force mapping and profiling on a sub 100-Å scale,” *Journal of Applied Physics*, **1987**, *61*, 4723–4729.
20. Zhong, Q.; Innis, D.; Kjoller, K.; Elings, V. B. “Fractured polymer/silica fiber surface studied by tapping mode atomic force microscopy,” *Surface Science Letters*, **1993**, *290*, L688–L692.
21. Magonov, S. N.; Elings, V.; Whangbo, M.-H. “Phase imaging and stiffness in tapping-mode atomic force microscopy,” *Surface Science*, **1997**, *375*, L385–L391.
22. Magonov, S. N.; Cleveland, J.; Elings, V.; Denley, D.; Whangbo, M.-H. “Tapping-mode atomic force microscopy study of the near-surface composition of a styrene-butadiene-styrene triblock copolymer film,” *Surface Science*, **1997**, *389*, 201–211.
23. Sarid, D. *Oxford Series in Optical and Imaging Sciences: Scanning Force Microscopy*; Oxford University Press: New York, 1991.
24. Ratner, B.; Tsukruk, V. V., Eds. *Scanning Probe Microscopy of Polymers, ACS Symposium Series Vol. 694*; American Chemical Society: Washington, DC, 1998.
25. Tsukruk, V. V.; Spencer, N. D., Eds. *Advances in Scanning Probe Microscopy of Polymers, Macromolecular Symposium Vol. 167*; Wiley-VCH: Weinheim, 2001.
26. Tsukruk, V. V. “Scanning probe microscopy of polymer surfaces,” *Rubber Chemistry and Technology*, **1997**, *70*, 430–467.
27. Magonov, S.; Reneker, D. H. “Characterization of polymer surfaces with atomic force microscopy,” *Annual Review of Materials Science*, **1997**, *27*, 175–222.
28. Giessibl, F. J. “Advances in atomic force microscopy,” *Reviews of Modern Physics*, **2003**, *75*, 949–983.

29. Roiter, Y.; Minko, S. “AFM single molecule experiments at the solid-liquid interface: In situ conformation of adsorbed flexible polyelectrolyte chains,” *Journal of the American Chemical Society*, **2005**, *127*, 15688–15689.
30. Julthongpiput, D.; Lin, Y.-H.; Teng, J.; Zubarev, E. R.; Tsukruk, V. V. “Y-Shaped amphiphilic brushes with switchable micellar surface structures,” *Journal of the American Chemical Society*, **2003**, *125*, 15912–15921.
31. Julthongpiput, D.; Lin, Y.-H.; Teng, J.; Zubarev, E. R.; Tsukruk, V. V. “Y-Shaped polymer brushes: nanoscale switchable surfaces,” *Langmuir*, **2003**, *19*, 7832–7836.
32. Lin, Y.-H.; Teng, J.; Zubarev, E. R.; Shulha, H.; Tsukruk, V. V. “In situ observation of switchable nanoscale topography for Y-Shaped binary brushes in fluids,” *Nano Letters*, **2005**, *5*, 491–495.
33. Sheiko, S. S.; Moller, M. “Visualization of macromolecules—a first step to manipulation and controlled response,” *Chemistry Reviews*, **2001**, *101*, 4099–4123.
34. Xu, H.; Shirvanyants, D.; Beers, K. L.; Matyjaszewski, K.; Dobrynin, A. V.; Rubinstein, M.; Sheiko, S. S. “Molecular visualization of conformation-triggered flow instability,” *Physical Review Letters*, **2005**, *94*, 237801.
35. Scheuring, S.; Seguin, J.; Marco, S.; Lévy, D.; Robert, B.; Rigaud, J.-L. “Nanodissection and high-resolution imaging of the *Rhodopseudomonas viridis* photosynthetic core complex in native membranes by AFM,” *Proceedings of the National Academy of Sciences U. S. A.*, **2003**, *100*, 1690–1693.
36. Engel, A.; Müller, D. J. “Observing single biomolecules at work with the atomic force microscope,” *Nature Structural Biology*, **2000**, *7*, 715–718.
37. Fotiadis, D.; Scheuring, S.; Müller, S. A.; Engel, A.; Müller, D. J. “Imaging and manipulation of biological structures with the AFM,” *Micron*, **2002**, *33*, 385–397.
38. Kumaki, J.; Kawauchi, T.; Yashima, E. “Reptational movements of single synthetic polymer chains on substrate observed by in situ atomic force microscopy,” *Macromolecules*, **2006**, *39*, 1209–1215.
39. Kolosov, O.; Yamanaka, K. “Nonlinear detection of ultrasonic vibrations in an atomic force microscope,” *Japanese Journal of Applied Physics*, **1993**, *32*, L1095–L1098.
40. Rabe, U.; Arnold, W. “Acoustic microscopy by atomic force microscopy,” *Applied Physics Letters*, **1994**, *64*, 1493–1495.
41. Dinelli, F.; Biswas, S. K.; Briggs, G. A. D.; Kolosov, O. V. “Measurements of stiff-material compliance on the nanoscale using ultrasonic force microscopy,” *Physical Review B*, **2000**, *61*, 13995–14006.
42. Rabe, U.; Amelio, S.; Kopycinska, M.; Hirsekorn, S.; Kempf, M.; Göken, M.; Arnold, W. “Imaging and measurement of local mechanical material properties by atomic force acoustic microscopy,” *Surface and Interface Analysis*, **2002**, *33*, 65–70.
43. Shekhawat, G. S.; Dravid, V. P. “Nanoscale imaging of buried structures via scanning near-field ultrasound holography,” *Science*, **2005**, *310*, 89–92.
44. Smith, D. P. E. “Limits of force microscopy,” *Review of Scientific Instruments*, **1995**, *66*, 3191–3195.
45. Tsukruk, V. V.; Gorbunov, V. V. “Nanomechanical analysis of polymer surfaces,” *Probe Microscopy*, **2002**, *241*, 3–4.
46. Ducker, W. A.; Senden, T. J.; Pashley, R. M. “Direct measurement of colloidal forces using an atomic force microscope,” *Nature*, **1991**, *353*, 239–241.
47. Butt, H.-J. “Measuring electrostatic, van der Waals, and Hydration forces in electrolyte solutions with an atomic force microscope,” *Biophysical Journal*, **1991**, *60*, 1438–1444.
48. McConney, M. E.; Anderson, K. D.; Brott, L. L.; Naik, R. R.; Tsukruk, V. V. “Bio-inspired material approaches to sensing,” *Advanced Functional Materials*, **2009**, *19*, 2527–2544.
49. Shulha, H.; Wong, C.; Kaplan, D. L.; Tsukruk, V. V. “Unfolding the multi-length scale domain structure of silk fibroin protein,” *Polymer*, **2006**, *47*, 5821–5830.
50. Tsukruk, V. V.; Bliznyuk, V. N. “Adhesive and friction forces between chemically modified silicon and silicon nitride surfaces,” *Langmuir*, **1998**, *14*, 446–455.

51. Zhang, W.; Zhang, X. "Single molecule mechanochemistry of macromolecules," *Progress in Polymer Science*, **2003**, *28*, 1271–1295.
52. Kühner, F.; Gaub, E. H. "Modelling cantilever-based force spectroscopy with polymers," *Polymer*, **2006**, *47*, 2555–2563.
53. Zou, S.; Korczagin, I.; Hempenius, M. A.; Schöherr, H.; Vancso, G. J. "Single molecule force spectroscopy of smart poly(ferrocenylsilane) macromolecules: Towards highly controlled redox-driven single chain motors," *Polymer*, **2006**, *47*, 2483–2892.
54. Al-Maawali, S.; Bemis, J. E.; Akhremitchev, B. B.; Liu, H.; Walker, G. C. "Single-molecule afm study of polystyrene grafted at gold surfaces," *The Journal of Adhesion*, **2005**, *81*, 999–1016.
55. Stroh, C.; Wang, H.; Bash, R.; Ashcroft, B.; Nelson, J.; Gruber, H.; Lohr, D.; Lindsay, S. M.; Hinterdorfer, P. "Single molecule recognition imaging microscopy," *Proceedings of the National Academy of Sciences U. S. A.*, **2004**, *101*, 12503–12507.
56. Zlatanova, J.; Lindsay, S. M.; Leuba, S. H. "Single molecule force spectroscopy in biology using the atomic force microscope," *Progress in Biophysics and Molecular Biology*, **2000**, *74*, 37–61.
57. Clausen-Schauman, H.; Seitz, M.; Krautbauer, R.; Gaub, H. E. "Force spectroscopy with single bio-molecules," *Current Opinion in Chemical Biology*, **2000**, *4*, 524–530.
58. VanLandingham, M. R.; Villarrubia, J. S.; Guthrie, W. F.; Meyers, G. F. "Nanoindentation of polymers: An overview," *Macromolecular Symposia*, **2001**, *167*, 15–43.
59. Vanlandingham, M. R.; McKnight, S. H.; Palmese, G. R.; Elings, J. R.; Huang, X.; Bogetti, T. A.; Eduljee, R. F.; Gillespie, J. W. "Nanoscale indentation of polymer systems using the atomic force microscope," *The Journal of Adhesion*, **1997**, *64*, 31–59.
60. Li, X.; Bhushan, B. "A review of nanoindentation continuous stiffness measurement technique and its applications," *Materials Characterization*, **2002**, *48*, 11–36.
61. Moeller, G. "AFM nanoindetation of viscoelastic materials with large end-radius probes," *Journal of Polymer Science Part B: Polymer Physics*, **2009**, *47*, 1573–1587.
62. Butt, H.-J.; Cappella, B.; Kappl, M. "Force measurements with the atomic force microscope: technique, interpretation, and applications," *Surface Science Reports*, **2005**, *59*, 1–152.
63. Cappella, B.; Dietler, G. "Force-distance curves by atomic force microscopy," *Surface Science Reports*, **1999**, *34*, 1–104.
64. Cleveland, J. P.; Manne, S.; Bocek, D.; Hansma, P. K. "A nondestructive method for determining the spring constant of cantilevers for scanning force microscopy," *Review of Scientific Instruments*, **1993**, *64*, 403–405.
65. Sader, J. E.; Chon, J. W. M.; Mulvaney, P. "Calibration of rectangular atomic force microscope cantilevers," *Review of Scientific Instruments*, **1999**, *70*, 3967–3969.
66. Sader, J. E. "Parallel beam approximation for v-shaped atomic force microscope cantilevers," *Review of Scientific Instruments*, **1995**, *66*, 4583–4587.
67. Hazel, J. L.; Tsukruk, V. V. "Spring constants of composite ceramic/gold cantilevers for scanning probe microscopy," *Thin Solid Films*, **1999**, *339*, 249–257.
68. Sader, J. E.; Larson, I.; Mulvaney, P.; White, L. R. "Method for the calibration of atomic force microscope cantilevers," *Review of Scientific Instruments*, **1995**, *66*, 3789–3798.
69. Gibson, C. T.; Watson, G. S.; Myhra, S. "Determination of the spring constants of probes for force microscopy/spectroscopy," *Nanotechnology*, **1996**, *7*, 259–262.
70. Hutter, J. L.; Bechhoefer, J. "Calibration of atomic force microscope tips," *Review of Scientific Instruments*, **1993**, *64*, 1868–1873.
71. Hazel, J.; Tsukruk, V. V. "Friction force microscopy measurements: Normal and torsional spring constants for V-shaped cantilevers," *Journal of Tribology*, **1998**, *120*, 814–819.
72. Matei, G. A.; Thoreson, E. J.; Pratt, J. R.; Newell, D. B.; Burnham, N. A. "Precision and accuracy of thermal calibration of atomic force microscopy cantilevers," *Review of Scientific Instruments*, **2006**, *77*, 083703.
73. Gibson, C. T.; Smith, D. A.; Roberts, C. J. "Calibration of silicon atomic force microscope cantilevers," *Nanotechnology*, **2005**, *16*, 234–238.

74. Machleidt, T.; Kästner, R.; Franke, K.-H. "Reconstruction and Geometric Assessment of AFM Tips", in *Nanoscale Calibration Standards and Methods: Dimensional and Related Measurements in Micro- and Nanometer Range*; Wilkening, G., Koenders, L., Eds.; Wiley-VCH: Weinheim, 2005; 297–310.
75. Czerkas, S.; Dziomba, T.; Bosse, H. "Comparison of Different Methods of SFM Tip Shape Determination for Various Characterization Structures and Types of Tip", in *Nanoscale Calibration Standards and Methods: Dimensional and Related Measurements in Micro- and Nanometer Range*; Wilkening, G., Koenders, L., Eds.; Wiley-VCH: Weinheim, 2005; 311–320.
76. Chizhik, S. A.; Huang, Z.; Gorbunov, V. V.; Myshkin, N. K.; Tsukruk, V. V. "Micro-mechanical properties of elastic polymeric materials as probed by scanning force microscopy," *Langmuir*, **1998**, *14*, 2606–2609.
77. Tsukruk, V. V.; Sidorenko, Y.; Gorbunov, V. V.; Chizhik, S. A. "Surface nanomechanical properties of polymer nanocomposite layers," *Langmuir*, **2001**, *17*, 6715–6719.
78. Stafford, C. M.; Harrison, C.; Beers, K. L.; Karim, A.; Amis, E. J.; Vanlandingham, M. R.; Kim, H.-C.; Volksen, W.; Miller, R. D.; Simony, E. E. "A Buckling-based metrology for measuring the elastic moduli of polymeric thin films," *Nature Materials*, **2004**, *3*, 545–550.
79. Jiang, C.; Singamaneni, S.; Merrick, E.; Tsukruk, V. V. "Complex buckling instability patterns of nanomembranes with encapsulated gold nanoparticle arrays," *Nano Letters*, **2006**, *6*, 2254–2259.
80. Markutsya, S.; Jiang, C.; Pikus, Y.; Tsukruk, V. V. "Free-standing multilayered nanocomposites films as highly sensitive nanomembranes," *Advanced Functional Materials*, **2005**, *15*, 771–780.
81. Higgins, M. J.; Proksch, R.; Sader, J. E.; Polcik, M.; Mc Endoo, S.; Cleveland, J. P.; Jarvis, S. P. "Noninvasive determination of optical lever sensitivity in atomic force micrscopy," *Review of Scientific Instruments*, **2006**, *77*, 013701.
82. Lin, D. C.; Horkay, F. "Nanomechanics of polymer gels and biological tissues: A critical review of analytical approaches in the hertzian regime and beyond," *Soft Matter*, **2008**, *4*, 669–682.
83. Lin, D. C.; Shreiber, D. I.; Dimitriadis, E. K.; Horkay, F. "Spherical indentation of soft matter beyond the hertzian regime: Numerical validation of hyperelastic models," *Biomechics and Modeling in Mechanobiology*, **2009**, *8*, 345–358.
84. Marti, O.; Hild, S. "Temperature-Dependent Surface Properties of Thin Polystyrene Films Determined by Scanning force Microscopy", in *Microstructure and Microtribology of Polymer Surface ACS Symposium Series 741*; Tsukruk, V.V., Wahl, K., Eds.; American Chemical Society: Washington, DC, 2000, pp. 212–226.
85. Aimé, J. P.; Elkaakour, Z.; Odin, C.; Bouhacina, T.; Michel, D.; Curely, J.; Dautant, A. "Comments on the use of the force mode in atomic force microscopy for polymer films," *Journal of Applied Physics*, **1994**, *76*, 754–762.
86. Choi, T.; Jang, J.-H.; Ullal, C. K.; LeMieux, M. C.; Tsukruk, V. V.; Thomas, E. L. "The elastic properties and plastic behavior of two-dimensional polymer structures fabricated by laser interference lithography," *Advanced Functional Materials*, **2006**, *16*, 1324–1330.
87. Jang, J.-H.; Ullal, C. K.; Choi, T.; LeMieux, M. C.; Tsukruk, V. V.; Thomas, E. L. "3D polymer microframes that exploit length-scale-dependent mechanical behavior," *Advanced Materials*, **2006**, *18*, 2123–2127.
88. Singamaneni, S.; Chang, S.; Jang, J.-H.; Davis, W.; Thomas, E. L.; Tsukruk, V. V. "Mechanical properties of composite polymer microstructures fabricated by interference lithography," *Physical Chemistry Chemical Physics*, **2008**, *10*, 4093–4105.
89. Julthongpiput, D.; LeMieux, M.; Tsukruk, V. V. "Micromechanical properties of glassy and rubbery polymer brush layers as probed by atomic force microscopy," *Polymer*, **2003**, *44*, 4557–4562.
90. Tsukruk, V. V.; Gorbunov, V. V.; Huang, Z.; Chizhik, S. A. "Dynamic microprobing of viscoelastic polymer properties," *Polymer International*, **2000**, *49*, 441–444.
91. Tsukruk, V. V.; Huang, Z. "Micro-thermomechanical properties of heterogeneous polymer films," *Polymer*, **2000**, *41*, 5541–5545.

92. Luzinov, I.; Julthongpiput, D.; Tsukruk, V. V. "Stability of microdomain morphology in tethered block copolymer monolayers," *Polymer*, **2001**, *42*, 2267–2273.
93. Kovalev, A.; Shulha, H.; LeMieux, M.; Myshkin, N.; Tsukruk, V. V. "Nanomechanical probing of layered nanoscale polymer films with atomic force microscopy," *Journal of Materials Research*, **2004**, *19*, 716–728.
94. Shulha, H.; Kovalev, A.; Myshkin, N.; Tsukruk, V. V. "Some aspects of AFM nanomechancal probing of surface polymer films," *European Polymer Journal*, **2004**, *40*, 949–956.
95. Shulha, H.; Zhai, X.; Tsukruk, V. V. "Molecular stiffness of individual hyperbranched macromolecules at solid surfaces," *Macromolecules*, **2003**, *36*, 2825–2831.
96. Tsukruk, V. V.; Shulha, H.; Zhai, X. "Nanoscale stiffness of individual dendritic molecules and their aggregates," *Applied Physics Letters*, **2003**, *82*, 907–909.
97. Kienberger, F.; Ebner, A.; Gruber, H. J.; Hinterdorfer, P. "Molecular recognition imaging and force spectroscopy of single biomolecules", *Accounts of Chemical Research*, **2006**, *39*, 29–36.
98. Engel, A.; Muller, D. J. "Observing single biomolecules at work with the atomic force microscope," *Nature Structural Biology*, **2000**, *7*, 715–718.
99. Hansma, H. G.; Kim, K. J.; Laney, D. E. "Properties of biomolecules measured from atomic force microscope images: A review," *Journal of Structural Biology*, **1997**, *119*, 99–108.
100. Fotiadis, D.; Scheuring, S.; Muller, S. A.; Engel, A.; Muller, D. J. "Imaging and manipulation of biological structures with the AFM", *Micron*, **2002**, *33*, 385–397.
101. Stolz, M.; Raiteri, R.; Daniels, A. U.; VanLandingham, M. R.; Baschong, W.; Aebi, U. "Dynamic elastic modulus of porcine articular cartilage determined at two different levels of tissue organization by indentation-type atomic force microscopy," *Biophysical Journal*, **2004**, *86*, 3269–3283.
102. Elkin, B. S.; Ilankovan, A.; Morrison, B. "Age dependent regional mechanical properties of the rat hippocampus and cortex," *Journal of Biomedical Engineering*, **2010**, *132*, 011010-1-10.
103. Shafieian, M.; Darcish, K. K.; Stone, J. R. "Changes to the viscoelastic properties of brain tissue after traumatic axonal injury," *Journal of Biomechanics*, **2009**, *42*, 2136–2142.
104. Harmon, M. E.; Kuckling, D.; Frank, C. W. "Photo-crosslinkable pnipaam copolymers. 5. Mechanical properties of hydrogel layers," *Langmuir*, **2003**, *19*, 10660–10665.
105. Braithwaite, G. J. C.; Luckham, P. F. "The simultaneous determination of the forces and viscoelastic properties of adsorbed polymer layers," *Journal of Colloid and Interface Science*, **1999**, *218*, 97–111.
106. Tripathy, S.; Berger, E. J. "Measuring viscoelasticity of soft samples using atomic force microscopy," *Journal of Biomechanical Engineering*, **2009**, *131*, 094507–094513.
107. Engler, A. J.; Sen, S.; Sweeney, H. L.; Discher, D. E. "Matrix elasticity directs stem cell lineage specification," *Cell*, **2006**, *126*, 677–689.
108. McConney, M. E.; Schaber, C. F.; Julian, M. D.; Barth, F. G.; Tsukruk, V. V. "Viscoelastic nanoscale properties of cuticle contribute to the high-pass properties of spider vibration receptor (*Cupoennius salei* keys)," *Journal of the Royal Society Interface*, **2007**, *4*, 1135–1143.
109. McConney, M. E.; Schaber, C. F.; Julian, M. D.; Eberhardt, W. C.; Humphrey, J. A. C.; Barth, F. G.; Tsukruk, V. V. "Surface force spectroscopic point load measurements and viscoelastic modeling of the micromechanical properties of air flow sensitive hairs of a spider (*Cupiennius salei*)," *Journal of the Royal Society Interface*, **2009**, *6*, 681–694.
110. Peleshanko, S.; Julian, M. D.; Ornatska, M.; McConney, M. E.; LeMieux, M. C.; Chen, N.; Tucker, C.; Yang, Y.; Liu, C.; Humphrey, J. A. C.; Tsukruk, V. V. "Hydrogel-encapsulated microfabricated haircells mimicking fish cupula neuromasts," *Advanced Materials*, **2007**, *19*, 2903–2909.
111. Yoshikawa, Y.; Yasuike, T.; Yagi, A.; Yamada, T. "Transverse elasticity of myofibrils of rabbit skeletal muscle studied by atomic force microscopy," *Biochemical and Biophysical Research Communications*, **1999**, *256*, 13–19.
112. Noy, A.; Vezenov, D. V.; Lieber, C. M. "Chemical force spectroscopy," *Annual Review of Materials Science*, **1997**, *27*, 381–421.

113. Noy, A. “Interaction at Solid-Fluid Interfaces”, In *Nanoscale Structure and Assembly at Solid-Fluid Interfaces*; Liu, X. Y., De Yoreo, J. J., Eds.; Kluwer Academic Publishers: Norwell, MA, 2004; 57–82.
114. Takano, H.; Kenseth, J. R.; Wong, S.-S.; O’Brien, J. C.; Porter, M. D. “Chemical and biochemical analysis using scanning force microscopy,” *Chemical Reviews*, **1999**, *99*, 2845–2890.
115. Janshoff, A.; Neitzert, M.; Oberdörfer, Y.; Fuchs, H. “Force-spectroscopy of molecular systems—single molecule spectroscopy of polymers and biomolecules,” *Angewandte Chemie International Edition*, **2000**, *39*, 3212–3237.
116. Noy, A., Ed. *Handbook of Molecular Force Spectroscopy*; Springer Science + Business Media, LLC: New York, 2008.
117. Thundat, T.; Zheng, X.-Y.; Chen, G. Y.; Warmack, R. J. “Role of relative humidity in atomic force microscopy imaging,” *Surface Science Letters*, **1993**, *294*, L939–L943.
118. Binggeli, M.; Mate, C. M. “Influence of capillary condensation on water on nanotribology studied by force microscopy,” *Applied Physics Letters*, **1994**, *65*, 415–417.
119. Fujihira, M.; Aoki, D.; Okabe, Y.; Takano, H.; Hokari, H.; Frommer, J.; Nagatani, Y.; Sakai, F. “Effect of capillary force on friction force microscopy: A scanning hydrophilicity microscope,” *Chemistry Letters*, **1996**, *25*, 499–502.
120. Noy, A.; Frisbie, C. D.; Rosznyai, L. F.; Wrighton, M. S.; Lieber, C. M. “Chemical force microscopy: Exploiting chemically modified yips to quantify adhesion, friction and functional group distributions in molecular assemblies,” *Journal of the American Chemical Society*, **1995**, *117*, 7943–7951.
121. Zhmud, B. V.; Golub, A. A. “Protolytic equilibria ligands immobilized at rigid matrix surfaces: A theoretical study,” *Colloid and Interface Science*, **1994**, *167*, 186–192.
122. Vezenov, D. V.; Noy, A.; Rozsnyai, L. F.; Lieber, C. M. “Force titrations and ionization state sensitive imaging of functional groups in aqueous solutions by chemical force microscopy,” *Journal of the American Chemical Society*, **1997**, *119*, 2006–2015.
123. Schönherr, H.; Hruska, Z.; Vancso, J. “Toward high resolution mapping of functional group distribution at surface treated polymers by AFM using modified tips,” *Macromolecules*, **2000**, *33*, 4532–4537.
124. Jiang, X.; Ortiz, C.; Hammond, P. T. “Exploring the rules for selective deposition: interactions of model polyamines on acid and oligioethylene oxide surfaces,” *Langmuir*, **2002**, *18*, 1131–1143.
125. Barber, A. H.; Cohen, S. R.; Wagner, H. D. “Measurement of carbon nanotube-polymer interfacial strength,” *Applied Physics Letters*, **2003**, *82*, 4140–4142.
126. Friddle, R. W.; LeMieux, M. C.; Cicero, G.; Artyukhin, A. B.; Tsukruk, V. V.; Grossman, J. C.; Galli, G.; Noy, A. “Single functional group interactions with individual carbon nanotubes,” *Nature Nanotechnology*, **2007**, *2*, 692–697.
127. Rosa-Zeiser, A.; Weilandt, E.; Hild, S.; Marti, O. “The simultaneous measurement of elastic, electrostatic, and adhesive properties by scanning force microscopy: Pulsed-force mode operation,” *Measurement Science and Technology*, **1997**, *8*, 1333–1338.
128. Marti, O.; Stifner, T.; Waschipky, H.; Quintus, M.; Hild, S. “Scanning probe microscopy of heterogenous polymers,” *Colloids and Surfaces A: Physicochemical and Engineering Aspects*, **1999**, *154*, 65–73.
129. Krotil, H.-U.; Stifter, T.; Waschipky, H.; Weishaupt, K.; Hild, S.; Marti, O. “Pulsed force mode: A new method for the investigation of surface properties,” *Surface and Interface Analysis*, **1999**, *27*, 336–340.
130. Carpick, R. W.; Salmeron, M. “Scratching the surface: Fundamental investigations of tribology with atomic force microscopy,” *Chemical Reviews*, **1997**, *97*, 1163–1194.
131. Bhushan, B. *Nanotribology and Nanomechanics: An Introduction*, 2nd ed.; Springer-Verlag: Berlin, 2008.
132. Cannara, R. J.; Brukman, M. J.; Cimatu, K.; Sumant, A. V.; Baldelli, S.; Carpick, R. W. “Nanoscale friction varied by isotopic shifting of surface vibrational frequencies,” *Science*, **2007**, *318*, 780–783.

133. Tsukruk, V. V. “Molecular lubricants and glues for micro- and nanodevices,” *Advanced Materials*, **2001**, *13*, 95–108.
134. Tsukruk, V. V.; Everson, M. P.; Lander, L. M.; Brittain, W. J. “Nanotribological properties of composite molecular films: C60 anchored to a self-assembled monolayer,” *Langmuir*, **1996**, *12*, 3905–3911.
135. Tsukruk, V. V.; Bliznyuk, V. N.; Hazel, J.; Visser, D.; Everson, M. P. “Organic molecular films under shear forces: Fluid and solid langmuir monolayers,” *Langmuir*, **1996**, *12*, 4840–4850.
136. Han, L.; Dean, D.; Ortiz, C.; Grodzinsky, A. J. “Lateral nanomechanics of cartilage aggrecan macromolecules,” *Biophysical. Journal*, **2007**, *92*, 1384–1398.
137. Tocha, E.; Schönher, H.; Vancso, G. J. “Surface relaxations of poly(methyl methacrylate) assesed by friction force microscopy on the nanoscale,” *Soft Matter*, **2009**, *5*, 1489–1495.
138. Majumdar, A. “Scanning thermal microscopy,” *Annual Review of Materials Science*, **1999**, *29*, 505–585.
139. Dinwiddie, R. B.; Pylkki, R. J.; West, P. E. “Thermal Conductivity Contrast Imaging with a Scanning Thermal Microscope”, in *Thermal Conductivity 22*; Tong, T. W., Ed.; Technomics Inc.: Lancaster, PA, 1994; 668–677.
140. Balk, L. J.; Maywald, M.; Pylkki, R. J. “Nanoscopic Detection of the Thermal Conductivity of Compound Semiconductor Materials by Enhanced Scanning Thermal Microscopy”, in *9th Conference on Microscopy of Semiconducting Materials (Inst. Phys. Conf. Ser. 146)*; Cullis, A. G., Staton-Bevan, A. E., Eds., IOP Publishing Ltd.: Bristol, England, 1995; 655–658.
141. Hammiche, A.; Hourston, D. J.; Pollock, H. M.; Reading, M.; Song, M. “Scanning thermal microscopy: Subsurface imaging, thermal mapping of polymer blends, and localized calorimetry,” *Journal of Vacuum Science and Technology B*, **1996**, *14*, 1486–1491.
142. Gorbunov, V. V.; Fuchigami, N.; Tsukruk, V. V. “Microthermal analysis with scanning thermal microscopy. I. Methodology and experimental,” *Probe Microscopy*, **2000**, *2*, 53–63.
143. Hammiche, A.; Pollock, H. M.; Song, M.; Hourston, D. J. “Sub-surface imaging by scanning thermal microscopy,” *Meas. Sci. Technol.*, **1996**, *7*, 142–150.
144. Pollock, H. M.; Hammiche, A.; Song, M.; Hourston, D. J.; Reading, M. “Interfaces in polymeric systems as studied by C.A.S.M.—a new combination of localised calorimetric analysis with scanning microscopy,” *The Journal of Adhesion*, **1998**, *67*, 217–234.
145. Price, D. M.; Reading, M.; Hammiche, A.; Pollock, H. M. “Micro-thermal analysis: Scanning thermal microscopy and localized thermal analysis,” *International Journal of Pharmaceutics*, **1999**, *192*, 85–96.
146. Price, D. M.; Reading, M.; Hammiche, A.; Pollock, H. M. “New adventures in thermal anaylsis,” *Journal of Thermal and Analytical Calorimetry*, **2000**, *60*, 723–733.
147. Pollock, H. M.; Hammiche, A. “Micro-thermal analysis: Techniques and applications,” *Journal of Physics D: Applied Physics*, **2001**, *34*, R23–R53.
148. Gorbunov, V. V.; Fuchigami, N.; Hazel, J. L.; Tsukruk, V. V. “Probing surface micro-thermal properties by scanning thermal microscopy,” *Langmuir*, **1999**, *15*, 8340–8343.
149. King, W. P.; Saxena, S.; Nelson, B. A.; Weeks, B. L.; Pitchimani, R. “Nanoscale thermal analysis of an energetic material,” *Nano Letters*, **2006**, *6*, 2145–2149.
150. Gorbunov, V. V.; Fuchigami, N.; Tsukruk, V. V. “Microthermal analysis with scanning thermal microscopy. II. Calibration, modeling, and interpretation,” *Probe Microscopy*, **2000**, *2*, 65–75.
151. Tsukruk, V.; Gorbunov, V.; Fuchigami, N. “Microthermal analysis of polymeric materials,” *Thermochimica Acta*, **2003**, *395*, 151–158.
152. Fischer, H. “Quantitative determination of heat conductivities by scanning thermal microscopy” *Thermochimica Acta*, **2005**, *425*, 69–74.
153. Lawson, N. S.; Ion, R. H.; Pollock, H. M.; Hourston, D. J.; Reading, M. “Characterising polymer surfaces—nanoindentation, surface force data, calorimetric microscopy,” *Physica Scripta*, **1994**, *T55*, 199–205.
154. Gorbunov, V. V.; Fuchigami, N.; Tsukruk, V. V. “Microthermal probing of ultrathin polymer films,” *High Performance Polymers*, **2000**, *12*, 603–610.

155. Chui, B. W.; Stowe, T. D.; Ju, Y. S.; Goodson, K. E.; Kenny, T. W.; Mamin, H. J.; Terris, B. D.; Ried, R. P.; Rugar, D. "Low-stiffness silicon cantilevers with integrated heaters and piezoresistive sensors for high-density AFM thermomechanical data storage," *Journal of Microelectromechanical Systems*, **1998**, *7*, 69–78.
156. Jones, K. J.; Kinshott, I.; Reading, M.; Lacey, A. A.; Nikolopoulos, C.; Pollock, H. M. "The origin and interpretation of the signals of MTDSC," *Thermochimica Acta*, **1997**, *305*, 187–199.
157. Häßler, R.; zur Müehlen, E. "An introduction to μTA$^{\text{TM}}$and its application to the study of interfaces," *Thermochimica Acta*, **2000**, *361*, 113–120.
158. Blaine, R. L.; Slough, C. G.; Price, D. M. "Microthermal Analysis Calibration, Repeatability and Reproducibility", in *Proceedings of the 27th NATAS*, Omnipress: Madison, WI, 1999; 691–696.
159. Meyers, G.; Pastzor, A.; Kjoller, K. "Localized thermal analysis: From the micro- to the nanoscale," *American Laboratory*, **2007**, *39*, 9–14.
160. Moon, I.; Androsch, R.; Chen, W.; Wunderlich, B. "The principles of micro-thermal analysis and its application to the study of macromolecules," *Journal of Thermal Analysis and Calorimetry*, **2000**, *59*, 187–203.
161. Forrest, J. A.; Dalnoki-Veress, K. "The glass transition in thin polymer films," *Advances in Colloid and Interface Science*, **2001**, *94*, 167–196.
162. Alcoutlabi, M.; McKenna, G. B. "Effects of confinement on material behavior at the nanometre size scale," *Journal of Physics: Condensed Matter*, **2005**, *17*, R461–R524.
163. Menczel, J. D.; Prime, R. B., Eds. *Thermal Analysis of Polymers: Fundamentals and Applications*; John Wiley & Sons: Hoboken, NJ, 2009.
164. Pruton, M. *Introduction to Surface Physics*; Oxford University Press: New York, 1994.
165. Hoppe, H.; Glatzel, T.; Niggemann, M.; Hinsch, A.; Lux-Steiner, M. C.; Sariciftci, N. S. "Kelvin probe force microscopy study on conjugated polymer/fullerene bulk heterojunction organic solar cells," *Nano Letters*, **2005**, *5*, 269–274.
166. Chiesa, M.; Bürgi, L.; Kim, J.-S.; Shikler, R.; Friend, R. H.; Sirringhaus, H. "Correlation between surface photovoltage and blend morphology in polyfluorene-based photodiodes," *Nano Letters*, **2005**, *5*, 559–563.
167. Zerweck, U.; Loppacher, C.; Otto, T.; Grafström, S.; Eng, L. M. "Accuracy and resolution limits of kelvin probe force microscopy," *Physical Review B*, **2005**, *71*, 125424.
168. Koley, G.; Spencer, G.; Bhangale, H. R. "Cantilever effects on the measurement of electrostatic potentials by scanning kelvin probe microscopy," *Applied Physics Letters*, **2001**, *79*, 545–547.
169. Gil, A.; Colchero Gómez-Herrero, J.; Baró, A. M. "Electrostatic force gradient signal: Resolution enhancement in electrostatic force microscopy and improved kelvin probe microscopy," *Nanotechnology*, **2003**, *14*, 332–340.
170. Takahashi, T.; Ono, S. "Tip-to-sample distance dependence of an electrostatic force in KFM measurements," *Ultramicroscopy*, **2004**, *100*, 287–292.
171. Sacha, G. M.; Verdaguer, A.; Martinez, J.; Sáenz, J. J.; Ogletree, D. F.; Salmeron, M. "Effective tip radius in electrostatic force microscopy," *Applied Physics Letters*, **2005**, *86*, 123101.
172. Argento, C.; French, R. H. "Parametric tip model and force-distance relation for hamaker constant determination from atomic force microscopy," *Journal of Applied Physics*, **1996**, *80*, 6081–6090.
173. Charrier, D. S. H.; Kemerink, M.; Smalbrugge, B. E.; de Vries, T.; Janssen, R. A. J. "Real versus measured surface potentials in scanning kelvin probe microscopy," *ACS Nano*, **2008**, *2*, 622–626.
174. Dai, H.; Wong, E.; Lieber, C. M. "Probing electrical transport in nanomaterials: Conductivity of individual carbon nanotubes," *Science*, **1996**, *272*, 523–526.
175. Klein, D. L.; McEuen, P. L. "Conducting atomic force microscopy of alkane layers on graphite," *Applied Physics Letters*, **1995**, *66*, 2478–2480.
176. O'Shea, S. J.; Atta, R. M.; Murrell, M. P.; Welland, M. E. "Conducting atomic force microscopy study of silicon dioxide breakdown," *Journal of Vacuum Science and Technology B*, **1995**, *13*, 1945–1952.

177. Kelley, T. W.; Granstrom, E. L.; Frisbie, C. D. "Conducting probe atomic force microscopy: a characterization tool for molecular electronics," *Advanced Materials*, **1999**, *11*, 261–264.
178. Pingree, L. S. C.; Hersam, M. C.; Kern, M. M.; Scott, B. J.; Marks, T. J. "Spatially-resolved electroluminescence of operating organic light-emitting diodes using conductive atomic force microscopy," *Applied Physics Letters*, **2004**, *85*, 344–346.
179. Ionescu-Zanetti, C.; Mechler, A.; Carter, S. A.; Lal, R. "Semiconductive polymer blends: correlating structure with transport properties at the nanoscale," *Advanced Materials*, **2004**, *16*, 385–389.
180. Douheret, O.; Lutsen, L.; Swinnen, A.; Breselge, M.; Vandewal, K.; Goris, L.; Manca, J. "Nanoscale electrical characterization of organic photovoltaic blends by conductive atomic force microscopy," *Applied Physics Letters*, **2006**, *89*, 032107.
181. Coffey, D. C.; Ginger, D. S. "Patterning phase separation in polymer films with Dip-Pen nanolithography," *Journal of the American Chemical Society*, **2005**, *127*, 4564–4565.
182. Coffey, D. C.; Reid, O. G.; Rodovsky, D. B.; Bartholomew, G. P.; Ginger, D. S. "Mapping local photocurrents in polymer/fullerene solar cells with photoconductive atomic force microscopy," *Nano Letters*, **2007**, *7*, 738–744.
183. Pingree, L. S. C.; MacLeod, B. A.; Ginger, D. S. "The changing face of PEDOT:PSS films: Substrate, bias, and processing effects on vertical charge transport," *Journal of Physical Chemistry C*, **2008**, *112*, 7922–7927.
184. Frenette, M.; MacLean, P. D.; Barclay, L. R. C.; Scaiano, J. C. "Radically different antioxidants: Thermally generated carbon-centered radicals as chain-breaking anti-oxidants," *Journal of the American Chemical Society*, **2006**, *128*, 16532–16539.
185. Reid, O. G.; Munechika, K.; Ginger, D. S. "Space charge limited current measurements on conjugated polymer films using conductive atomic force microscopy," *Nano Letters*, **2008**, *8*, 1602–1609.
186. Porthun, S.; Abelmann, L.; Lodder, C. "Magnetic force microscopy of thin film media for high-density magnetic recording," *Journal of Magnetism and Magnetic Materials*, **1998**, *182*, 238–273.
187. Folks, L.; Woodward, R. C. "The use of MFM for investigating domain structures in modern permanent magnet materials," *Journal of Magnetism and Magnetic Materials*, **1998**, *190*, 28–41.
188. Kleiber, M.; Kümmerlen, F.; Löhndorf, M.; Wadas, A.; Wiesendanger, R. "Magnetization switching of submicrometer Co dots induced by a magnetic force microscope tip," *Physical Review B*, **1998**, *58*, 5563–5567.
189. Gider, S.; Shi, J.; Awschalom, D. D.; Hopkins, P. F.; Campman, K. F.; Gossard, A. C.; Kent, A. D.; von Molnar, S. "Imaging and magnetometry of switching in nanometer-scale iron particles," *Applied Physics Letters*, **1996**, *69*, 3269–3271.
190. Bliznyuk, V.; Singamaneni, S.; Sahoo, S.; Polisetty, S.; He, X.; Binek, C. "Self-assembly of magnetic ni nanoparticles into 1D arrays with antiferromagnetic order," *Nanotechnology*, **2009**, *20*, 105606.
191. Proksch, R. B.; Schaffer, T. E.; Moskowitz, B. M.; Dahlberg, E. D.; Bazylinski, D. A.; Frankel, R. B. "MFM of the submicron magnetic assembly in magnetotactic bacterium," *Applied Physics Letters*, **1995**, *66*, 2582–2584.
192. Yan, L.; Shen, S.; Li, W.; Wang, X. "Dipolar chains and 2D aligned stripes of polymer-coated magnetic iron colloid," *Journal of Applied Polymer Science*, **2006**, *101*, 4211–4215.
193. Sun, S.; Anders, S.; Hamann, H. F.; Thiele, J.-U.; Baglin, J. E. E.; Thomson, T.; Fullerton, E. E.; Murray, C. B.; Terris, B. D. "Polymer mediated self-assembly of magnetic nanoparticles," *Journal of the American Chemical Society*, **2002**, *124*, 2884–2885.
194. Lillehei, P. T.; Park, C.; Rouse, J. H.; Siochi, E. J. "Imaging carbon nanotubes in high performance polymer composites via magnetic force microscopy," *Nano Letters*, **2002**, *2*, 827–829.